

Manuscript Number: LITHOS8730R3

Title: Early Devonian mafic igneous rocks in the East Kunlun Orogen, NW China: Implications for the transition from the Proto- to Paleo-Tethys oceans

Article Type: Regular Article

Keywords: Mafic igneous rocks; Post-collisional; Early continental rifting; Proto- and Paleo-Tethys oceans; East Kunlun

Corresponding Author: Dr. Jinlong Dong, Ph.D.

Corresponding Author's Institution: Peking University

First Author: Jinlong Dong, Ph.D.

Order of Authors: Jinlong Dong, Ph.D.; Shuguang Song, Ph.D.; Li Su, Ph.D.; Mark B. Allen, Ph.D.; Yanguang Li, Master; Chao Wang, Ph.D.

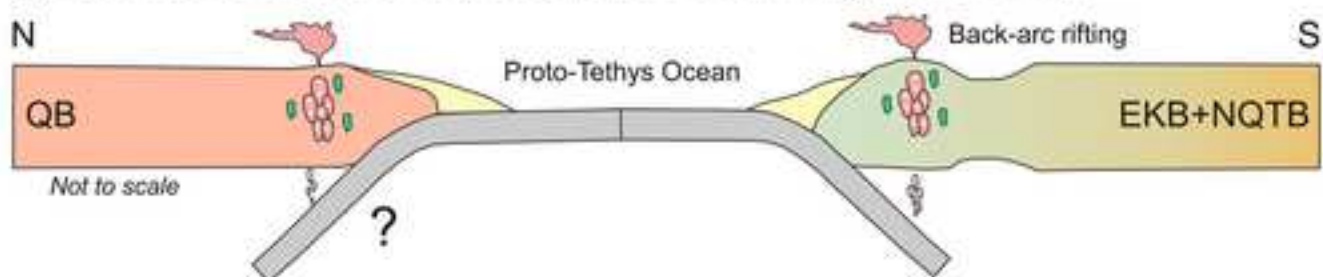
Abstract: The tectonic evolution of the Proto- and Paleo-Tethys oceans had a significant influence on ocean-continent distributions in East Asia in the Phanerozoic, and major implications for continental growth in the region. However, it remains ambiguous when and how the Proto-Tethys Ocean transformed into the Paleo-Tethys Ocean. Here we present petrologic, mineralogical, chronological and geochemical data for Early Devonian mafic igneous rocks, located in the East Kunlun Orogen. The mafic igneous rocks include basaltic lavas and diabase dykes, and are tholeiitic in composition. Geochemical and Sr-Nd isotopic data indicate that the basaltic lavas were derived from melting of a spinel-bearing asthenospheric mantle (E-MORB) at normal mantle potential temperatures (1384-1400 °C) with negligible (1-4%) crustal contamination. The diabase dykes probably originated from melting of a spinel-bearing lithospheric mantle metasomatized by subduction-related fluids, with 5-20% crustal contamination, and crystallized at 1100-1135 °C. Both basaltic lavas and diabase dykes have the geochemical characteristics of within-plate basalts. Magmatic zircons from the mafic rocks yield Early Devonian ages (407-403 Ma), postdating the East Kunlun ultrahigh-pressure metamorphism by 19-25 Myr. Comparing our results with the location and timing of the high- and ultrahigh-pressure metamorphic belt, we conclude that the mafic igneous rocks formed in a post-collisional extensional setting. Their generation was associated with both the terminal stages of the Proto-Tethys orogenic belt, (with orogenic collapse promoted by repeated and localized delamination of lithospheric mantle), and early continental rifting related to the evolution of the Paleo-Tethys Ocean to the south. The period of ~426-390 Ma is important for the transition from Proto- to Paleo-Tethys oceans in the East Kunlun Orogen.

Research Data Related to this Submission

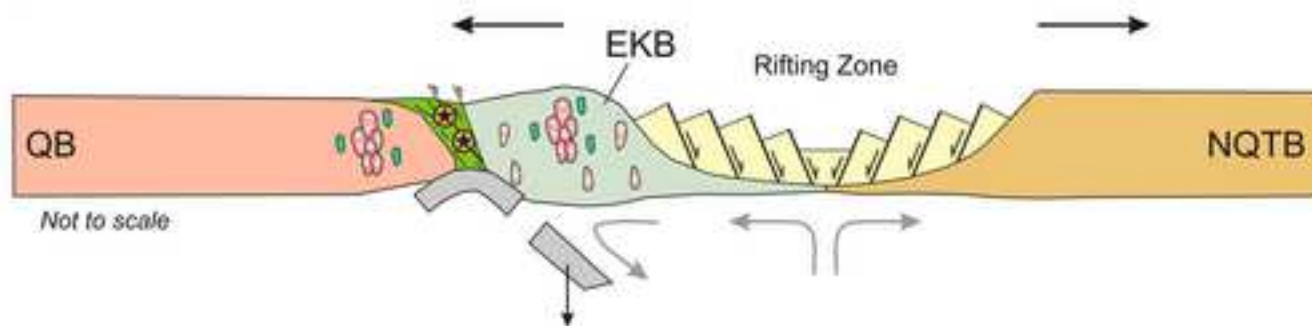
-----  
There are no linked research data sets for this submission. The following reason is given:

Data will be made available on request

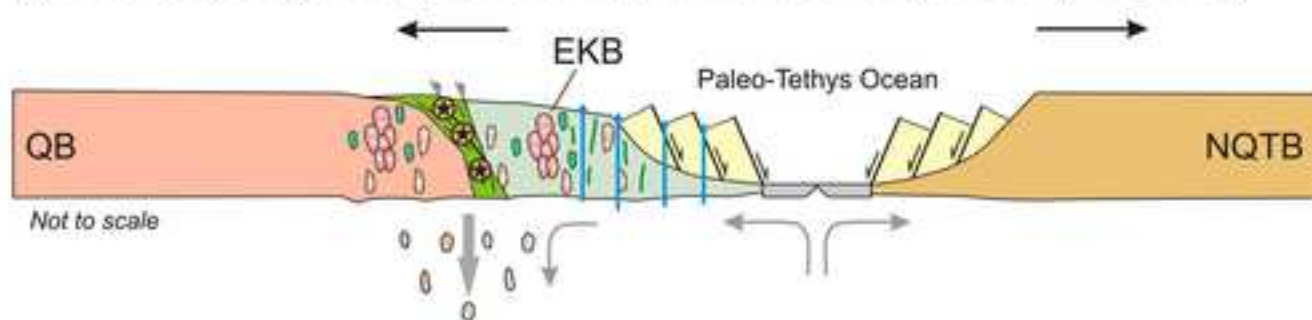
(A) Subduction of the Proto-Tethys Ocean and back-arc rifting (>480-428 Ma)



(B) Closure and slab break-off of the Proto-Tethys Ocean (428-413 Ma)



(C) Proto-Tethys orogen collapse and formation of the Paleo-Tethys Ocean (413-380 Ma)



- The Tatu mafic rocks have geochemical features similar to within-plate basalts.
- The Tatu mafic rocks (407-403 Ma) formed in a post-collisional extensional setting.
- The period of ~426-390 Ma is important for the transition from the Proto- to Paleo-Tethys oceans.

1 **Early Devonian mafic igneous rocks in the East Kunlun**  
2 **Orogen, NW China: Implications for the transition from the**  
3 **Proto- to Paleo-Tethys oceans**

4 Jinlong Dong <sup>a</sup>, Shuguang Song <sup>a\*</sup>, Li Su <sup>b</sup>, Mark B. Allen <sup>c</sup>, Yanguang Li <sup>d</sup>,  
5 Chao Wang <sup>e</sup>

6

7 <sup>a</sup> *MOE Key Laboratory of Orogenic Belts and Crustal Evolution, School of Earth and Space*  
8 *Sciences, Peking University, Beijing 100871, China*

9 <sup>b</sup> *School of Scientific Research and State Key Laboratory of Geological Processes and Mineral*  
10 *Resources, China University of Geosciences, Beijing 100083, China*

11 <sup>c</sup> *Department of Earth Sciences, University of Durham, Durham DH1 3LE, UK*

12 <sup>d</sup> *Xi'an Center of Geological Survey, China Geological Survey, Xi'an 710054, China*

13 <sup>e</sup> *School of Earth Sciences and Resources, China University of Geosciences, Beijing 100083,*  
14 *China*

15

16 \* [Corresponding author:](#)

17 \*[Shuguang Song](#)

18 [Email: sgsong@pku.edu.cn](mailto:sgsong@pku.edu.cn)

19 Manuscript for *Lithos*

## 20 **Abstract**

21       The tectonic evolution of the Proto- and Paleo-Tethys oceans had a significant  
22 influence on ocean-continent distributions in East Asia in the Phanerozoic, and major  
23 implications for continental growth in the region. However, it remains ambiguous  
24 when and how the Proto-Tethys Ocean transformed into the Paleo-Tethys Ocean. Here  
25 we present petrologic, mineralogical, chronological and geochemical data for Early  
26 Devonian mafic igneous rocks, located in the East Kunlun Orogen. The mafic igneous  
27 rocks include basaltic lavas and diabase dykes, and are tholeiitic in composition.  
28 Geochemical and Sr-Nd isotopic data indicate that the basaltic lavas were derived  
29 from melting of a spinel-bearing asthenospheric mantle (E-MORB) at normal mantle  
30 potential temperatures (1384-1400 °C) with negligible (1-4%) crustal contamination.  
31 The diabase dykes probably originated from melting of a spinel-bearing lithospheric  
32 mantle metasomatized by subduction-related fluids, with 5-20% crustal contamination,  
33 and crystallized at 1100-1135 °C. Both basaltic lavas and diabase dykes have the  
34 geochemical characteristics of within-plate basalts. Magmatic zircons from the mafic  
35 rocks yield Early Devonian ages (407-403 Ma), postdating the East Kunlun  
36 ultrahigh-pressure metamorphism by 19-25 Myr. Comparing our results with the  
37 location and timing of the high- and ultrahigh-pressure metamorphic belt, we  
38 conclude that the mafic igneous rocks formed in a post-collisional extensional setting.  
39 Their generation was associated with both the terminal stages of the Proto-Tethys  
40 orogenic belt, (with orogenic collapse promoted by repeated and localized  
41 delamination of lithospheric mantle), and early continental rifting related to the

42 evolution of the Paleo-Tethys Ocean to the south. The period of ~426-390 Ma is  
43 important for the transition from Proto- to Paleo-Tethys oceans in the East Kunlun  
44 Orogen.

45 *Keywords:* Mafic igneous rocks; Post-collisional; Early continental rifting; Proto- and  
46 Paleo-Tethys oceans; East Kunlun

## 47 **1. Introduction**

48 The Proto-Tethys Ocean originally separated continental blocks that are now  
49 present across China and SE Asia, from the Qiangtang and Sibumasu blocks to the  
50 south and east, to the Tarim and North China blocks to the north (Li et al., 2018). The  
51 opening of Proto-Tethys was probably related to the break-up of Rodinia at ~750 Ma,  
52 and its closure resulted from the assembly of Gondwana during the Silurian to Early  
53 Devonian (Li et al., 2008a; von Raumer and Stampfli, 2008; Zhao et al., 2018a; Song  
54 et al., 2018). The Paleo-Tethys Ocean separated the European and Asiatic Hunic  
55 terranes and Gondwana (Metcalf, 2013; Zhao et al., 2018a). Several studies have  
56 suggested that the Paleo-Tethys Ocean started to open in the Devonian, and its final  
57 closure occurred at ~220 Ma (Jian et al., 2009; Zhai et al., 2011, 2013; Song et al.,  
58 2020). The tectonic evolution of the Proto- and Paleo-Tethys oceans clearly played  
59 key roles in the assembly of the East Asian blocks in Pangea (Li et al., 2018; Zhao et  
60 al., 2018a). However, it is still not well constrained when and how the demise of  
61 Proto-Tethys related to the opening of Paleo-Tethys. To address this issue, it is useful  
62 to understand the final stages of the Proto-Tethys orogenic belt, and to decipher the  
63 early continental rifting related to the opening of Paleo-Tethys.

64 It is generally accepted that the East Kunlun Orogen (EKO) was a product of the  
65 tectonic evolution of the Proto- and Paleo-Tethys oceans (Bian et al., 2004; Chen et al.,  
66 2017, 2020; Dong et al., 2018a). Based on high- to ultrahigh-pressure (HP-UHP)  
67 metamorphic rocks, recent studies have proposed that the collision event between the  
68 East Kunlun and Qaidam blocks could represent the final closure of the Proto-Tethys  
69 Ocean (Bi et al., 2018; Song et al., 2018). Therefore, study of the EKO could provide  
70 important clues for the late stage evolution of the Proto-Tethys orogenic belt.  
71 However, the Middle Silurian to Middle Devonian evolution of the EKO is  
72 controversial; both large scale lithospheric delamination and oceanic slab break-off  
73 have been proposed as causes of regional extension (Zhang et al., 2014; Zhong et al.,  
74 2017; Xin et al., 2018; Chen et al., 2020). Xiong et al. (2014) proposed that the  
75 formation of the Paleo-Tethys Ocean started at ~393 Ma, based on within-plate mafic  
76 dykes in the EKO, however, the dataset of that study is limited and the early evolution  
77 of Paleo-Tethys needs to be re-evaluated.

78 The geochemistry of mafic igneous rocks can provide important clues for  
79 deciphering the nature and composition of their mantle source, and the tectonic setting  
80 of melt generation and emplacement (Wilson, 1989; Melluso et al., 2006; Zhu et al.,  
81 2008; Lee et al., 2009; Prelević et al., 2012; Song et al., 2015a). In this contribution,  
82 we present new petrologic, mineralogical, chronological and geochemical studies for  
83 the basaltic lavas and diabase dykes in the EKO. We propose that these mafic igneous  
84 rocks formed in a post-collisional setting, consistent with extension, and that they  
85 relate to the final collapse of the Proto-Tethys orogenic belt and early continental

86 rifting related to the opening of the Paleo-Tethys Ocean.

## 87 **2. Geological background**

88 The EKO is located between the Songpan-Ganzi Terrane and the Qaidam Block  
89 on the northeastern margin of the Tibetan Plateau (Fig. 1A). It has dimensions of  
90 ~1500 km west-east with a south-north width of ~50-200 km (Fig. 1B). To the south,  
91 the Songpan-Ganzi Terrane consists mainly of Late Triassic granitoids (Yuan et al.,  
92 2010) and Mesozoic submarine fan and deep marine rocks formed in the Paleo-Tethys  
93 Ocean (Ding et al., 2013). To the north, the Qaidam Block predominantly consists of  
94 Mesozoic to Cenozoic sedimentary rocks overlying a Precambrian basement (e.g., Xia  
95 et al., 2001). The Precambrian basement, primarily exposed at the southern and  
96 northern margins of the Qaidam Block, mainly consists of granitic and pelitic gneisses,  
97 granitoids, amphibolites and marbles (e.g., Wan et al., 2006).

98 The EKO is an important tectonic junction linking the Qinling Orogen to the east  
99 and the West Kunlun Orogenic Belt to the west (Fig. 1A). It experienced a long and  
100 complicated tectonic evolution associated with the Proto- and Paleo-Tethys oceans  
101 from the Cambrian to the Triassic (Li et al., 2018; Dong et al., 2018a; Song et al.,  
102 2018). The EKO consists of: (1) the A'nyemaqen accretionary belt, (2) extensive  
103 granitoids, (3) Precambrian basement and (4) an Early Paleozoic complex (Fig. 1B).  
104 In the south of the EKO, the A'nyemaqen accretionary belt (Fig. 1B) consists of  
105 tectonic mélanges and ophiolites in a matrix of strongly deformed Permian turbidites  
106 (Pei et al., 2018). Based on chronological data, two major episodes of ophiolites,  
107 dated at 516-450 Ma and 345-333 Ma, are recognized in the A'nyemaqen accretionary



108 belt, representing fragments of the ancient Tethys oceans (Bian et al., 2004; Dong et  
109 al., 2018a; Pei et al., 2018). In the north of the EKO is the Early Paleozoic complex  
110 (Fig. 1B), which primarily consists of eclogites, 537-421 Ma ophiolites, and  
111 arc-related igneous rocks (e.g., Yang et al., 1996; Meng et al., 2013; Jiang et al., 2015;  
112 Song et al., 2018). The eclogites in the Early Paleozoic complex formed at 432-411  
113 Ma, and occur as interlayers and lenses in a schist matrix (Meng et al., 2013; Qi et al.,  
114 2014; Song et al., 2018). The eclogites at Kehete have coesite inclusions and  
115 pseudomorphs (Song et al., 2018; Bi et al., 2018), indicating the presence of HP-UHP  
116 metamorphism in the EKO. Thus, the Early Paleozoic complex in the EKO is also a  
117 HP-UHP metamorphic belt (Fig. 1B). Precambrian basement rocks are widespread in  
118 the EKO and they show a wide age range from Paleoproterozoic to Neoproterozoic  
119 (He et al., 2016; Song et al., 2018). The granitoids cover an area of more than 48,000  
120 km<sup>2</sup> and they primarily formed in the Early Paleozoic and Triassic (e.g., Chen et al.,  
121 2017, 2020; Xin et al., 2018).

122 The study area is located in the Early Paleozoic complex, at the easternmost part  
123 of the EKO (Fig. 1B). The geology of this region includes Precambrian  
124 meta-sedimentary rocks, the Early Paleozoic subduction complex, Silurian-Devonian  
125 and Mesozoic volcanic-sedimentary strata, Ordovician-Devonian and  
126 Permian-Triassic granitoids and ultramafic rocks (Fig. 2A) (BGQP, 1973). The  
127 Precambrian meta-sedimentary rocks are composed of dolomitic limestone, marble,  
128 sandstone and schist with minor granulite (BGQP, 1973). The Silurian-Devonian  
129 volcanic-sedimentary strata (~6.5 km thick in the study area; Fig. 2B) consist mainly

130 of carbonate, sandstone, slate, pyroclastic rock and volcanic rock (BGQP, 1973). The  
131 Mesozoic volcanic-sedimentary strata contain carbonate, conglomerate, sandstone and  
132 pyroclastic rock, with minor coal beds. The Silurian-Devonian volcanic-sedimentary  
133 strata have fault contacts with the Precambrian meta-sedimentary rocks and Mesozoic  
134 volcanic-sedimentary strata (Fig. 2B). The Ordovician-Devonian granitoids consist  
135 mainly of syenogranite and granodiorite, showing geochemical features similar to  
136 A<sub>2</sub>-type granite (Chen et al., 2020).

### 137 **3. Field relations and petrography**

138 The studied mafic igneous rocks are from the Tatu area (Fig. 1); sample  
139 locations and sampling horizons are shown in Fig. 2A and 2B, respectively. The rocks  
140 are basaltic lavas and diabase dykes and their contact relationships cannot be directly  
141 observed in the field (Figs. 2A and 3). Basaltic lavas are gray to dark gray in color,  
142 and have a massive structure with a thickness of ~70-150 m (Figs. 2B, 3A and 3B).  
143 Thin section observations indicate that the basaltic lavas are mainly basalts, with  
144 minor amounts of dolerite. Contact relationship between the basalts and dolerites are  
145 conformable in the field (Fig. 3B). The basalts are variously altered, but original  
146 textures are still present (Fig. 3C and D). They are porphyritic with clinopyroxene  
147 (5-10 vol.%) and plagioclase (3-5 vol.%) phenocrysts in a matrix of oriented fine- to  
148 micro-grained plagioclase, clinopyroxene, opaque minerals and altered minerals (e.g.,  
149 chlorite and epidote) (Fig. 3C and D). The dolerites show a fine-grained ophitic  
150 texture and are primarily composed of clinopyroxene (35-55 vol.%) and plagioclase  
151 (45-60 vol.%) with minor opaques and altered minerals (Fig. 3E).

152 The two diabase dykes can be found in the study area. These dykes are dark gray  
153 in color and possess a massive structure. The dykes are almost vertical, and typical  
154 E-W trending. They can be traced for distances of 50-250 m with a width of ~1.5-20  
155 m (Fig. 3F and G). The dykes have intrusive contacts with the Precambrian  
156 meta-sedimentary rocks (Fig. 3F and G). There is slight alteration, and ophitic  
157 textures (Fig. 3H and I). The compositions are 20-35 vol.% clinopyroxene, 60-75 vol.%  
158 plagioclase, and minor altered minerals (Fig. 3H and I). Clinopyroxene grains are  
159 irregular to subhedral crystals varying from 0.1 to 1.5 mm in size, and occurring  
160 interstitially between plagioclase grains (Fig. 3H and I). Clinopyroxene crystals are  
161 locally altered to epidote, chlorite and actinolite. Plagioclase grains are euhedral to  
162 subhedral laths and vary in size (0.25-2.5 mm) with well-developed polysynthetic  
163 twinning (Fig. 3H and I). Some plagioclase grains are mottled in appearance, and  
164 altered to kaolin or sericite.

## 165 **4. Analytical methods**

### 166 **4.1 Mineral chemistry**

167 Mineral analyses for major element oxides, including clinopyroxene and  
168 plagioclase, were done on a JEOL JXA-8230 Electron Probe Microanalyzer (EPMA)  
169 at the Laboratory of Orogenic Belts and Crustal Evolution of Peking University.  
170 Analytical conditions were optimized for standard silicates and oxides at 15 kV  
171 accelerating voltage with a 10 nA focused beam current for all the elements. Routine  
172 analyses were obtained by counting for 30 s at peak and ~15 s on background.  
173 Repeated analysis of natural and synthetic mineral standards yielded precisions better

174 than  $\pm 2\%$  for most elements.

## 175 **4.2 Whole-rock major and trace element analyses**

176 Whole-rock major and trace element analysis was performed at the Geological  
177 Lab Center of China University of Geosciences, Beijing (CUGB). Whole-rock major  
178 element oxides were done using inductively coupled plasma-atomic emission  
179 spectroscopy (ICP-OES). The analytical uncertainties are usually less than 1% for  
180 most elements with the exception of  $\text{TiO}_2$  (~1.5%) and  $\text{P}_2\text{O}_5$  (~2.0%) based on  
181 Chinese national geological standard reference materials GSR-1 and GSR-3, and US  
182 Geological Survey rock standards AGV-2 and W-2. Loss on ignition (LOI) was  
183 obtained by placing 1000 mg of samples in the furnace at 1000 °C for three hours  
184 before being cooled in a desiccator and reweighed. Whole-rock trace elements were  
185 determined on an Agilent-7500a inductively coupled plasma-mass spectrometry  
186 (ICP-MS). Rock standards AGV-2 (US Geological Survey), and GSR-1, GSR-3,  
187 GSR-5 (national geological standard reference materials of China) were used to  
188 monitor the analytical accuracy and precision. The analytical accuracy, as indicated by  
189 relative difference between measured and recommended values, is better than 5% for  
190 most elements, 10-13% for U, Th, Sc, Er, Nb and Cu, and 10-15% for Gd, Ta and Tm.  
191 More detailed analytical procedures are presented in [Dong et al. \(2018b\)](#).

## 192 **4.3 Zircon U-Pb geochronology**

193 Zircons were separated from one dolerite sample (17KL-25) and one diabase  
194 dyke sample (18KL-63) by using standard density and magnetic separation techniques  
195 and selected by handpicking under a binocular microscope. Cathodoluminescence

196 (CL) examination was conducted using an FEI QUANTA650 FEG Scanning Electron  
197 Microscope (SEM) under conditions of 15 kV/120 nA at MOE Key Laboratory of  
198 Orogenic Belt and Crustal Evolution, Peking University.

199 Measurements of U, Th and Pb in zircons were performed on an Agilent-7700x  
200 quadrupole inductively coupled plasma mass spectrometry coupled with a Coherent  
201 Geolas Pro laser sampler (LA-ICP-MS) at the Laboratory Center, Xi'an Center of  
202 Geological Survey, China. Laser spot size of 25  $\mu\text{m}$ , laser energy density of 6.0  $\text{J}/\text{cm}^2$   
203 and a repetition rate of 5 Hz were applied for analysis. Helium was used as a carrier  
204 gas to transport the ablated aerosol to the LA-ICP-MS. Each analysis spot comprised  
205 about 10 s background measurements and 40 s of sample measurements. National  
206 Institute of Standards and Technology 610 glass, zircon standard 91500 and TEM  
207 were used for calibration. The software GLITTER 4.4.1 (Macquarie University) was  
208 used to process the isotopic ratios and element concentrations of zircon grains. The  
209 common Pb correction was made following [Andersen \(2002\)](#). Age calculations and  
210 plots of concordia diagrams were done using Isoplot 3.0 ([Ludwig, 2003](#)).

#### 211 **4.4 Whole-rock Sr-Nd isotope analyses**

212 Whole-rock Sr-Nd isotope analyses were determined at MOE Key Laboratory of  
213 Orogenic Belts and Crustal Evolution, Peking University. About 200 mg of the  
214 unknown sample and ~150 mg of the standard sample (BCR-2) were dissolved by  
215 using  $\text{HF}+\text{HNO}_3$  in hermetic Teflon jars and heated at 140  $^\circ\text{C}$  for seven days in order  
216 to be well dissolved. Separation and purification of the whole-rock Sr-Nd isotope  
217 were achieved using conventional cation columns (AG50W and P507). The

218 whole-rock Sr-Nd isotope analyses were performed on the Micromass Isoprobe  
219 multi-collector ICP-MS (MC-ICP-MS). Standard sample BCR-2 was used to evaluate  
220 the separation and purification process of Rb, Sr, Sm, and Nd. Mass fractionation  
221 corrections for  $^{87}\text{Sr}/^{86}\text{Sr}$  and  $^{143}\text{Nd}/^{144}\text{Nd}$  ratios were normalized to  $^{86}\text{Sr}/^{88}\text{Sr}=0.1194$   
222 and  $^{146}\text{Nd}/^{144}\text{Nd}=0.7219$ , respectively.

## 223 **5. Results**

### 224 **5.1 Mineral chemistry**

225 As the minerals in the basaltic lavas are not fresh (Fig. 3C and D), we only  
226 obtain chemical compositions of plagioclase and clinopyroxene from the Tatu  
227 diabase dykes. Representative plagioclase and clinopyroxene compositions of the  
228 diabase dykes are given in Table S1 and Table S2, respectively. The plagioclases in  
229 the diabase dykes show a wide compositional range and their anorthite contents vary  
230 from 36.74 to 71.75 wt.% (Fig. 4A; Table S1). The clinopyroxenes in the diabase  
231 dykes are mainly augites, with a formula of  $\text{Wo}_{37.1-43.7}\text{En}_{37.4-45.7}\text{Fs}_{13.4-19.7}$  (Fig. 4B;  
232 Table S2). Their Mg# [ $100 \times \text{Mg}^{2+}/(\text{Mg}^{2+} + \text{Fe}^{2+})$ ] varies from 67 to 78 (Table S2), and  
233 is not correlated with  $\text{Cr}_2\text{O}_3$  (not shown). The clinopyroxenes are characterized by  
234 high  $\text{TiO}_2$  (0.82-1.62 wt.%),  $\text{MgO}$  (12.85-16.09 wt.%), low  $\text{Al}_2\text{O}_3$  (2.88-4.85 wt.%),  
235  $\text{Cr}_2\text{O}_3$  (0-0.07 wt.%),  $\text{Na}_2\text{O}$  (0.35-0.59 wt.%) and  $\text{K}_2\text{O}$  (0-0.04 wt.%) (Table S2). The  
236 clinopyroxene compositions are consistent with those of rift-related igneous rocks  
237 (Fig. 4B and C). In the  $\text{Al}_Z$  versus  $\text{TiO}_2$  diagram (Fig. 4C), the clinopyroxene  
238 compositions show a rift-related trend.

## 239 **5.2 Whole-rock major and trace element data**

240 Thirteen basaltic lavas and twelve diabase dykes were analyzed for whole-rock  
241 major and trace elements; results are listed in [Table S3](#). Thin section observations  
242 indicate that the basaltic lavas and diabase dykes have undergone varying degrees of  
243 low-grade greenschist facies metamorphism during post-magmatic processes ([Fig. 3C](#),  
244 D, E, H and I). This metamorphism might have modified the contents of fluid-mobile  
245 elements (e.g., Ca, K, Na, Rb, Sr and Cs). As a consequence, we have used the  
246 immobile elements (e.g., REEs and HFSEs), some major elements (e.g., Si, Fe, Mg,  
247 Ti and Al), transitional elements (e.g., Cr, Ni and V) and Nd isotopic data for rock  
248 classification and discussion of the petrogenesis. Given the relatively high mobility of  
249 Sr and Rb, Sr isotopic data are used and interpreted with caution.

250 The Tatu basaltic lavas show varying SiO<sub>2</sub> (47.83-53.31 wt.%, normalized to an  
251 anhydrous basis), FeO<sub>T</sub> (12.21-16.58 wt.%), relatively high MgO (5.17-8.50 wt.%),  
252 medium to high TiO<sub>2</sub> (1.40-2.62 wt.%), low Mg# (40-54), Cr (38-188 ppm) and Ni  
253 (47-115 ppm) values ([Table S3](#)). The diabase dykes have variable SiO<sub>2</sub> (48.61-55.67  
254 wt.%), high TiO<sub>2</sub> (2.11-3.06 wt.%), FeO<sub>T</sub> (10.60-12.52 wt.%), low MgO (3.73-4.83  
255 wt.%), Cr (2-29 ppm) and Ni (4-19 ppm) contents ([Table S3](#)). In the Zr/TiO<sub>2</sub> versus  
256 Nb/Y diagram ([Fig. 5A](#)), all of the samples plot in the sub-alkaline basalt field. In the  
257 TiO<sub>2</sub> versus FeO<sub>T</sub>/MgO diagram ([Fig. 5B](#)), the Tatu mafic igneous rocks show a  
258 tholeiitic trend. The basaltic samples have low ratios of Ti/Y (280-463) and Sm/Yb  
259 (1.23-1.82), whereas the diabase dyke samples show low Ti/Y (299-377) and  
260 relatively high Sm/Yb (2.13-3.03) ([Fig. 5C](#); [Table S3](#)).

261 The Tatuio basaltic lavas show a large range of total REE contents (47-103 ppm)  
262 and possess similar chondrite-normalized REE patterns, with varying LREE  
263 enrichment [ $La_N/Yb_N=1.55-2.89$ ; hereafter, subscript N denotes normalized to the  
264 chondrite values of Sun and McDonough (1989)], weak HREE depletion  
265 ( $Gd_N/Yb_N=1.25-1.75$ ) and insignificant Eu anomalies ( $Eu/Eu^*=0.89-0.97$ ) (Fig. 6A).  
266 In the primitive mantle-normalized multi-element diagrams (Fig. 6B), the basaltic  
267 lavas are characterized by weak “humped” patterns with varying enrichment in U, Ta  
268 and REEs and lack negative Nb anomalies. The Tatuio basaltic lavas show  
269 geochemical affinities similar to the present-day E-MORB, and their trace element  
270 patterns are also similar to those of the low-Ti basalts in Deccan Traps of India (Fig.  
271 6A and B).

272 The Tatuio diabase dykes have consistent chondrite-normalized REE patterns  
273 with obvious LREE enrichment ( $La_N/Yb_N=7.34-10.50$ ), moderate HREE depletion  
274 ( $Gd_N/Yb_N=1.79-2.26$ ) and discernible negative Eu anomalies ( $Eu/Eu^*=0.81-0.88$ ) (Fig.  
275 6C). In the primitive mantle-normalized multi-element diagrams (Fig. 6D), the  
276 diabase dyke samples display enrichment in Th, U and LREEs with obvious negative  
277 Nb-Ta and Ti anomalies. Their geochemical features of trace elements are different  
278 from those of OIB, E-MORB, N-MORB and island arc basalts (Fig. 6C and D).

### 279 **5.3 Zircon U-Pb ages**

280 Two samples, including 17KL-25 (basaltic lava) and 18KL-63 (diabase dyke),  
281 were selected for zircon U-Pb age studies. The results of LA-ICP-MS U-Pb zircon  
282 analyses are given in Table S4. The cathodoluminescence (CL) images and zircon



283 U-Pb concordia plots are shown in [Fig. 7](#).

284 Zircon grains from lava sample 17KL-25, which is dolerite, are mainly subhedral  
285 to euhedral, colorless and transparent crystals. They have prismatic shapes (20-120  
286  $\mu\text{m}$  long) with length-to-width ratios of 1.2:1-3:1 ([Fig. 7A](#) and B). The CL images  
287 indicate that these zircons have straight and wide oscillatory growth bands, which is  
288 typical of zircons from mafic igneous rocks (e.g., [Song et al., 2015a](#); [Dong et al.,](#)  
289 [2018b](#)). Zircons from sample 17KL-25 have variable concentrations of U (120-874  
290 ppm) and Th (66-824 ppm), with high Th/U ratios that vary from 0.33 to 1.08  
291 (average of 0.59) ([Table S4](#)). Five analyzed spots with Th/U ratios of 0.46-0.68 yield  
292 relatively old apparent  $^{206}\text{Pb}/^{238}\text{U}$  ages of 452-431 Ma, with a weighted mean of 439.6  
293  $\pm 3.5$  Ma (MSWD=0.17; [Fig. 7A](#)). We interpret that these zircons are xenocrysts and  
294 the age of  $\sim 440$  Ma is consistent with the timing of arc magmatism in the EKO (e.g.,  
295 [Jiang et al., 2015](#)). Sixteen analyzed spots yield apparent  $^{206}\text{Pb}/^{238}\text{U}$  ages of 425-395  
296 Ma with a weighted mean of  $407.0 \pm 3.9$  Ma (MSWD=2.3; [Fig. 7B](#)), which is  
297 interpreted as the eruption time of the Tatu basaltic lavas.

298 Most zircon grains from the diabase dyke sample (18KL-63) are sub-rounded,  
299 rounded and oval in morphology and show equant to long prismatic shapes (20-150  
300  $\mu\text{m}$  long) with length-to-width ratios of 1:1-3.5:1 ([Fig. 7C](#)). CL images indicate that  
301 these zircons are mainly light to dark grey with clear oscillatory zoning. Some zircons  
302 have inherited cores and overgrown rims ([Fig. 7C](#)). Twelve analyses were conducted  
303 on these zircons and yield old apparent  $^{206}\text{Pb}/^{238}\text{U}$  ages of 2447-467 Ma ([Table S4](#)),  
304 which are likely to be xenocrysts. Three zircon grains are subhedral to euhedral, and

305 stubby (30-60  $\mu\text{m}$  long with length-to-width ratios of 1.2:1-1.8:1) (Fig. 7C). CL  
306 images show that the three zircon grains have straight and wide oscillatory growth  
307 bands (Fig. 7C), typical of zircons derived from mafic magmas. The three zircons  
308 show various concentrations of U (546-727 ppm) and Th (283-458 ppm) with high  
309 Th/U ratios varying from 0.43 to 0.63 (Table S4). They yield the youngest apparent  
310  $^{206}\text{Pb}/^{238}\text{U}$  ages of 406-400 Ma with a weighted mean of  $402.7 \pm 4.8$  Ma  
311 (MSWD=0.58; Fig. 7D). Thus, we interpret the age of  $\sim 403$  Ma to represent the  
312 emplacement timing of the diabase dykes, which is coeval, within error, with the  
313 basaltic lavas.

#### 314 **5.4 Whole-rock Sr-Nd isotope data**

315 Eight basaltic lava and four diabase dyke samples were analyzed for whole-rock  
316 Sr-Nd isotopic compositions. The results are listed in Table S5 and plots of  $\epsilon_{\text{Nd}}(t)$   
317 versus  $I_{\text{Sr}}(t)$  are displayed in Fig. 8A. Initial isotopic ratios of basaltic lavas and  
318 diabase dykes were calculated at 407 Ma and 403 Ma, respectively. Both the basaltic  
319 lava and diabase dyke samples show relatively wide ranges of the whole-rock Sr-Nd  
320 isotopic compositions (Table S5; Fig. 8A). The basaltic lavas show weakly to  
321 moderately positive  $\epsilon_{\text{Nd}}(t)$  values (+1.27 to +4.65) with initial  $^{87}\text{Sr}/^{86}\text{Sr}$  ratios ranging  
322 from 0.70359 to 0.71041. Several basaltic samples (11KL-02, 05, 39 and 41 and  
323 17KL-25) exhibit a trend towards high Sr isotope values at a constant  $\epsilon_{\text{Nd}}(t)$  value,  
324 which is likely to be due to alteration by hydrothermal fluids (Fig. 8A). The diabase  
325 dyke samples have moderately negative  $\epsilon_{\text{Nd}}(t)$  values (-4.54 to -1.88) and relatively  
326 high initial  $^{87}\text{Sr}/^{86}\text{Sr}$  ratios ranging between 0.70886 to 0.71513. Notably, the diabase

327 dyke samples do not show a trend parallel to abscissa axis with increasing  $I_{Sr}(t)$ ,  
328 indicating that late alteration could be insignificant (Fig. 8A). Two-stage depleted  
329 mantle model ages ( $T_{DM2}$ ) of the basaltic lavas vary from 769 Ma to 1044 Ma,  
330 whereas the  $T_{DM2}$  ages of the diabase dykes are much older, in the range of 1298-1513  
331 Ma (Table S5). In the  $\epsilon_{Nd}(t)$  versus Mg# diagram (Fig. 8B), the basaltic lavas show a  
332 moderately segmented trend, suggesting significant fractional crystallization and  
333 limited crustal contamination during magma evolution and migration. The obvious  
334 negative correlations between  $\epsilon_{Nd}(t)$  and Mg# (Fig. 8B) indicate that the diabase dyke  
335 samples were strongly affected by crustal contamination.

## 336 **6. Discussion**

### 337 **6.1 Petrogenesis**

#### 338 6.1.1 Fractional crystallization

339 In general, primary magmas generated from mantle peridotites should have high  
340 Cr (300-500 ppm), Ni (300-400 ppm) and Mg# values (68-76) (Frey et al., 1978;  
341 Wilson, 1989). All the Tatuio mafic igneous rocks are characterized by low Cr (2-188  
342 ppm), Ni (4-115 ppm) and Mg# values (37-54) (Table S3), indicating fractional  
343 crystallization of olivine, pyroxene and spinel during the magmatic evolution. For the  
344 basaltic lavas, the possible fractional crystallization can also be observed in the flat  
345 trend of the  $\epsilon_{Nd}(t)$  versus Mg# diagram (Fig. 8B). Negative correlations of MgO and  
346  $FeO_T$  with  $SiO_2$  (Fig. 9A and B) imply that the primary magmas of both the basaltic  
347 lavas and diabase dykes experienced fractional crystallization of mafic minerals. For  
348 the basaltic lavas, the relatively poor correlation between  $Al_2O_3$  and  $SiO_2$  ( $r=0.55$ ; Fig.

349 9C) implies limited fractionation of plagioclase, consistent with the insignificant Eu  
350 anomalies ( $\text{Eu}/\text{Eu}^*=0.89\text{-}0.97$ ) (Fig. 6A). In contrast, for the diabase dykes, the  
351 strongly negative correlation of  $\text{Al}_2\text{O}_3$  with  $\text{SiO}_2$  ( $r=0.94$ ; Fig. 9C) indicates possible  
352 plagioclase crystallization, supported by the negative Eu anomalies  
353 ( $\text{Eu}/\text{Eu}^*=0.81\text{-}0.88$ ) (Fig. 6C). In addition, Fe-Ti oxide crystallization plays an  
354 important role in the evolution of the basaltic lavas, which is suggested by the  
355 negative correlation between  $\text{TiO}_2$  and MgO (Fig. 9D). For the diabase dykes,  
356 fractionation of Fe-Ti oxides can be discounted, due to the absence of a negative  
357 correlation between  $\text{TiO}_2$  and MgO (Fig. 9D). The obvious correlations of Ni and V  
358 with Cr (Fig. 9E and F) indicate that primary magmas of both the basaltic lavas and  
359 diabase dykes underwent significant fractionation of clinopyroxene. Hornblende  
360 crystallization can be discounted for both the basaltic lavas and diabase dykes,  
361 because of the absence of MREE depletion (Fig. 6A and C). In summary, the basaltic  
362 lavas underwent fractionation of clinopyroxene, Fe-Ti oxide and minor plagioclase,  
363 whereas the diabase dykes likely experienced fractionation of clinopyroxene and  
364 plagioclase.

#### 365 6.1.2 Crustal contamination

366 It is important to evaluate the potential role of crustal contamination in the Tatuo  
367 mafic igneous rocks. Contamination appears to be limited for the Tatuo basaltic lavas  
368 because: (1) crustal contamination could give rise to negative Nb-Ta and positive  
369 Zr-Hf anomalies (Zhou et al., 2007), but the basaltic lavas are characterized by  
370 slightly negative to positive Nb anomalies [ $\text{Nb}_{\text{PM}}/\text{La}_{\text{PM}}=0.70\text{-}1.01$ ; hereafter, subscript

371 PM denotes normalized to the primary mantle values of [Sun and McDonough \(1989\)](#)],  
372 positive Ta anomalies ( $Ta_{PM}/Th_{PM}=0.93-2.59$ ) and slightly negative Zr-Hf anomalies  
373 ([Fig. 6B](#)); (2) in the Th/Yb versus Nb/Yb diagram ([Fig. 10A](#)), all the basaltic samples  
374 plot within the MORB-OIB array; (3) in the Nb/Th versus Nb/La diagram ([Fig. 10B](#)),  
375 the basaltic samples do not show a crustal contamination trend; and (4) the presence  
376 of moderately segmented trends between  $\epsilon_{Nd}(t)$  and Mg# ([Fig. 8B](#)) for the basaltic  
377 lavas also confirms the limited effect of crustal contamination.

378 By comparison, the influence of crustal contamination is very significant for the  
379 Tatuio diabase dykes, due to the presence of the prominent negative correlation  
380 between  $\epsilon_{Nd}(t)$  and Mg# ([Fig. 8B](#)). Crustal contamination can also be inferred by the  
381 abundant zircons captured by the mafic dykes (see above). It is worth noting that the  
382 upper continental crust is more enriched in Th compared to lower and middle  
383 continental crusts ([Rudnick and Gao, 2003](#)), indicating that the crustal contaminant  
384 for the Tatuio diabase dykes could be derived from the upper continental crust.

### 385 6.1.3 Mantle source

386 Mafic igneous rocks were generally derived from either lithospheric mantle or  
387 asthenospheric mantle ([George and Rogers, 2002](#); [Dong et al., 2019](#)). Rocks derived  
388 from the lithospheric mantle are characterized by low  $\epsilon_{Nd}(t)$  values and high initial  
389  $^{87}Sr/^{86}Sr$  ratios, whereas those from the asthenospheric mantle have depleted  
390 signatures in isotopes (e.g., [Dong et al., 2019](#)). In our study, although some basaltic  
391 samples (17KL-25 and 11KL-02, 05, 39 and 41) show relatively high initial  $^{87}Sr/^{86}Sr$   
392 ratios due to the subsequent alteration ([Fig. 8A](#)), all the basaltic lavas are

393 characterized by high  $\epsilon_{Nd}(t)$  (+1.27 to +4.65) and slightly enriched in LREEs and  
394 HFSEs with insignificant crustal contamination (Figs. 6A-B and 8B). These pieces of  
395 evidence indicate that the basaltic lavas could be derived from the asthenospheric  
396 mantle and show geochemical affinities with E-MORB (Hofmann, 1997). In the  
397 Th/Yb versus Nb/Yb and Nb/Zr versus Th/Zr diagrams (Fig. 10A and C) the entire  
398 basaltic sample set plots within the MORB-OIB array, and close to E-MORB.

399 By comparison, the diabase dyke samples are characterized by negative  $\epsilon_{Nd}(t)$   
400 (-4.54 to -1.88) and high initial  $^{87}Sr/^{86}Sr$  (0.70886 to 0.71513) with  $T_{DM2}$  ages of  
401 1298-1513 Ma (Table S5), implying that they originated from the lithospheric mantle.  
402 Moreover, the Zr/Nb (15.90-31.76), Th/Ta (10.41-15.30) and La/Nb (3.26-4.04)  
403 values of the diabase dykes are far higher than those of MORB (Sun and McDonough,  
404 1989), further confirming their derivation from the lithospheric mantle. In general, the  
405 continental crust has negative Nb/Nb\* anomalies (0.23-0.55)  
406  $[Nb/Nb^* = Nb_{PM}/(Th_{PM} \times La_{PM})^{1/2}]$  and low Nb/La ratios (0.39-0.63) with positive Zr-Hf  
407 anomalies (Rudnick and Gao, 2003). In the Tatu case, the diabase dyke samples  
408 show much lower Nb/Nb\* (0.18-0.21) and Nb/La (0.25-0.29) values than those of the  
409 continental crust, indicating that their mantle source could be more complicated. For  
410 the diabase dykes, the negative Zr-Hf anomalies (Fig. 6D), especially for sample  
411 17KL-72 and 18KL-63, indicate that their mantle source could have been  
412 metasomatized by subduction-related fluids/melts. The inference could be  
413 demonstrated in the Th/Yb versus Nb/Yb and Nb/Th versus Nb/La diagrams (Fig.  
414 10A and B): the diabase dykes plot outside of the MORB-OIB array and show very

415 limited variation ranges, indicating that they inherit the features of a mantle source  
416 previously metasomatized by subduction-related fluids/melts. In the Nb/Zr versus  
417 Th/Zr diagram (Fig. 10C), the diabase dyke samples significantly deviate from the  
418 MORB-OIB array, reflecting the influence of slab-derived fluids.

419 To further determine the type of mantle source and effect of crustal  
420 contamination for the Tatuo mafic igneous rocks, we utilize the simple binary mixing  
421 model proposed by DePaolo (1981) and Zhou et al. (2007). In this modeling, we make  
422 the following assumptions: (1) the Wanbaogou sandstone from the EKO represents  
423 the crustal end member; (2) the Xiarihamu mafic-ultramafic intrusion in the EKO  
424 represents the subcontinental lithospheric mantle source; and (3) the E-MORB glasses  
425 from the Gakkel Ridge proposed by Mühe et al. (1997) represents the asthenospheric  
426 mantle source. As shown in Fig. 10D, the calculation results indicate that the basaltic  
427 lavas were derived from asthenospheric mantle (E-MORB) with insignificant (<4%)  
428 crustal contamination, whereas the diabase dykes were originated from subcontinental  
429 lithospheric mantle with various degrees (5-20%) of crustal contamination.

430 Ratios of REEs in basaltic lavas are used to distinguish the nature of the mantle  
431 source and roughly estimate the degree of melting (e.g., George and Rogers, 2002). In  
432 this study, we use the method suggested by George and Rogers (2002) to determine  
433 the nature of mantle source for the Tatuo mafic igneous rocks. As shown in Fig. 11A,  
434 the basaltic lavas have low ratios of La/Yb (2.16-4.03) and Tb/Yb (0.25-0.33),  
435 indicating that they were possibly produced by 5-7% partial melting of spinel-bearing  
436 mantle source. However, as mentioned above, the diabase dykes have been

437 significantly affected by crustal contamination and slab-derived fluids. In those  
438 processes, LREEs might be significantly changed, but HREEs could be inactive (e.g.,  
439 [Green, 2006](#)). Thus, the low ratios of Tb/Yb (0.31-0.38) from the diabase dykes  
440 indicate a spinel-bearing mantle source ([Fig. 11A](#)).

#### 441 6.1.4 Mantle/crystallization temperature

442 Among the basaltic lavas, samples 17KL-21, 22 and 25 are the least-evolved  
443 with the highest MgO (8.29-8.50 wt.%) and Mg# (~54). For these samples, we invoke  
444 the method of [Lee et al. \(2009\)](#) to estimate the main oxide components for the  
445 primitive magmas and the mantle potential temperature ( $T_p$ ). The calculation results  
446 show that the primitive magmas are high-Mg basaltic compositions with 48.08-50.45  
447 wt.% SiO<sub>2</sub>, 9.36-9.63 wt.% FeO<sub>T</sub> and 12.74-13.21 wt.% MgO. The resulting  $T_p$  varies  
448 from 1384 °C to 1400 °C. The mantle potential temperatures are very close to those of  
449 the typical upper mantle (1350 °C) ([Davies, 2009](#)).

450 For the diabase dykes, on account of the significant effects of crustal  
451 contamination and slab-derived fluids (see above), we use clinopyroxene-only  
452 thermometers proposed by [Nimis and Taylor \(2000\)](#) to give an approximate estimate  
453 of the crystallization temperature. In the calculation, we adopt the hypothesis that the  
454 high-Mg (Mg#>75) clinopyroxenes within the diabase dykes could be in equilibrium  
455 with the primitive magmas. Applying this method, the calculated crystallization  
456 temperature is between 1100 °C and 1135 °C for the Tatuio diabase dykes.

## 457 **6.2 Tectonic setting of the EKO during ~426-390 Ma**

458 Mafic igneous rocks can occur in multiple tectonic settings, such as mid-ocean



459 ridges, subduction zones and within-plate regimes (e.g., [Wilson, 1989](#)). The Tatu  
460 mafic igneous rocks exhibit high  $\text{TiO}_2$  (1.40-3.06 wt.%), Zr (70-282 ppm), V  
461 (179-459 ppm), Zr/Y (3.0-6.0) and Zr/Sm (23.3-30.0), similar to those of the  
462 within-plate mafic rocks ([Wilson, 1989](#); [Li et al., 2008b](#)). In the V versus Ti/1000  
463 diagram ([Fig. 11B](#)), the mafic rock samples mainly plot in the continental flood  
464 basalts (CFB) field. The affinities of within-plate basalts can also be observed by trace  
465 element patterns and clinopyroxene compositions ([Figs. 4B, 4C and 6](#)). However, the  
466 calculated mantle and crystallization temperatures (1100-1400 °C) for the Tatu mafic  
467 igneous rocks are far less than those of the Hawaiian picrites (1500-1600 °C) ([Lee et  
468 al., 2009](#)), indicating that they are not associated with a mantle-plume event.

469 Several studies have proposed that the EKO records the evolution of the  
470 Proto-Tethys Ocean from early Cambrian subduction, to oceanic closure, to  
471 continental collision (e.g., [Qi et al., 2014](#); [Dong et al., 2018a](#); [Song et al., 2018](#); [Bi et  
472 al., 2018](#)). The UHP metamorphic ages in the EKO are mainly clustered at 428-426  
473 Ma ([Song et al., 2018](#)), which represents the final closure of the Proto-Tethys Ocean  
474 ([Song et al., 2018](#); [Bi et al., 2018](#)) and are before the formation of the Tatu mafic  
475 igneous rocks (407-403 Ma). Given these timings, the Tatu mafic igneous rocks  
476 could have formed in a syn- or post-collisional setting. However, syn-collisional  
477 magmatic rocks are mainly originated from both oceanic and continental crust with  
478 rare mantle-derived components (e.g., [Song et al., 2015b](#)), such as the Xitieshan  
479 syn-collisional granites ([Zhao et al., 2017](#)). We therefore propose that the Tatu mafic  
480 igneous rocks could form in a post-collisional extensional setting. Recent studies have

481 showed that ~412-392 Ma mafic igneous rocks with within-plate basalt features and  
482 ~426-390 Ma A<sub>2</sub>-type granitoids are distributed in other places in the EKO, such as  
483 Weibao, Haxiya and Wulonggou, and also interpret a post-collisional extensional  
484 setting (Yang et al., 2014; Zhong et al., 2017; Xin et al., 2018; Chen et al., 2020).  
485 Taking the spatial and temporal relations and tectonic settings of these ~426-390 Ma  
486 igneous rocks into consideration, we suggest that the whole EKO was in the  
487 post-collisional extensional setting during ~426-390 Ma.

### 488 **6.3 Geodynamic Implications**

489 In general, lithospheric mantle is relatively cold, and only melts to generate  
490 mafic magma if there is involvement of an additional heat source. For most  
491 post-collisional settings, the asthenospheric mantle is considered as the potential heat  
492 source (Zhao et al., 2018b). It is generally accepted that involvement of the  
493 asthenospheric mantle in melting in post-collisional settings results from one or more  
494 of the following: slab break-off, wholesale convective removal of the lithosphere,  
495 lithosphere delamination, and small-scale sublithospheric convection (e.g., Bird, 1979;  
496 Houseman et al., 1981; von Blanckenburg and Davies, 1995; Kaislaniemi et al., 2014;  
497 Zhu et al., 2015; Zhao et al., 2018b). In our case, any proposed tectono-magmatic  
498 model for the Tatuo mafic igneous rocks in the EKO must be able to explain the  
499 following features: (1) the volume is relatively small; (2) the mantle source for the  
500 basaltic lavas was the asthenospheric mantle; (3) the mantle source for the diabase  
501 dykes could be the lithospheric mantle metasomatized by slab-derived fluids; and (4)  
502 the mafic igneous rocks show within-plate geochemical affinities. In addition, the

503 tectono-magmatic model must also be responsible for the following observations: (1)  
504 as shown in Fig. 11C, peak magmatism in the EKO occurred at ~423 Ma, postdating  
505 the UHP metamorphism with a very short time interval (~3-5 Myr); (2) the A<sub>2</sub>-type  
506 granitoids at the magmatic peak period could possibly be created with input of  
507 asthenosphere-derived components (Fig. 11D); and (3) the mafic igneous rocks in the  
508 EKO, dated at ~412-392 Ma (e.g., Yang et al., 2014; Xiong et al., 2014; Zhong et al.,  
509 2017), are scattered and have small volumes, such as the Weibao, Haxiya, Yuejinshan  
510 and Tatu examples.

511 Slab break-off occurs due to the contrasting buoyancy and tensile forces,  
512 between the resistant, buoyant, continental lithosphere and subducting oceanic  
513 lithosphere (von Blanckenburg and Davies, 1995). The model predicts a linear zone of  
514 magmatism along the orogenic belt, occurring ~1-10 Myr after continental collision  
515 (e.g., von Blanckenburg and Davies, 1995; Macera et al., 2008). In this model, the  
516 magmatism is variable in composition, and includes bimodal volcanic rocks, A<sub>2</sub>-type  
517 felsic rocks and within-plate mafic rocks (e.g., von Blanckenburg and Davies; Zhu et  
518 al., 2015). The model is reasonable to explain two of the observations of the  
519 post-collisional magmatism in the EKO: (1) peak magmatism postdated the UHP  
520 metamorphism by ~3-5 Myr (Fig. 11C), and (2) the possible input of  
521 asthenosphere-derived components started at ~423 Ma, synchronous with peak  
522 magmatism (Fig. 11D). However, the slab break-off model does not explain the  
523 temporally- and spatially-scattered style and volumes of the mafic magmatism in the  
524 EKO, dated at ~412-392 Ma (e.g., Yang et al., 2014; Xiong et al., 2014; Zhong et al.,

525 [2017](#)). In addition, the model does not explain the relatively long-term (~20 Myr)  
526 mafic within-plate magmatism in the EKO.

527 Convective removal of the lithosphere involves a regional detachment of the  
528 lower lithosphere ([Houseman et al., 1981](#); [Morency et al., 2002](#)). The model has been  
529 used to explain the potassic and ultrapotassic rocks of orogenic plateaux (e.g., [Song et](#)  
530 [al., 2015b](#)), such as the 15.6-4.5 Ma volcanic rocks in Southwestern Anatolia, Turkey  
531 ([Prelević et al., 2012](#)). However, the lack of extensive potassic and ultrapotassic rocks  
532 in the EKO argues against the model of wholesale convective removal of the  
533 lithosphere.

534 The delamination model predicts that the lithospheric mantle peels away with or  
535 without portion of the eclogitic lower crust, resulting in the upwelling of heated  
536 asthenosphere and crust-mantle interaction ([Bird, 1979](#)). Lithospheric delamination  
537 would give rise to extensive lower and middle crustal melting as well as formation of  
538 massive amounts of asthenosphere-derived rocks. However, the lack of lower  
539 crust-derived rocks, such as adakites and tonalites, and large-scale  
540 asthenosphere-derived mafic igneous rocks rule out the delamination model for the  
541 EKO.

542 The small-scale sublithospheric convection model predicts that previous  
543 subduction resulted in wetting of the lower lithosphere and upper asthenosphere and a  
544 decrease in mantle viscosity, which gave rise to repeated and localized delamination  
545 of the lowermost lithosphere and upwelling of asthenosphere ([Kaislaniemi et al., 2014](#);  
546 [Kheirkhah et al., 2015](#)). Results from numerical modeling indicate that the small-scale

547 lithospheric delamination could not be observed by seismic tomography at depths far  
548 shallower than 100 km (Kaislaniemi et al., 2014). In the model, the igneous rocks may  
549 have geochemical features similar to within-plate rocks (e.g., Kheirkhah et al., 2015).  
550 The model can explain long-term magmatic activities which display no clear patterns  
551 in space and time (Kaislaniemi et al., 2014). The model is reasonable to explain the  
552 spatially and temporally scattered pattern of the mafic igneous rocks dated at  
553 ~412-392 Ma in the EKO (e.g., Yang et al., 2014; Xiong et al., 2014; Zhong et al.,  
554 2017). In summary, we propose that the final collapse of the Proto-Tethys orogenic  
555 belt was induced by the repeated and localized delamination of lithospheric mantle  
556 during ~412-390 Ma.

557         There is commonly a time lag of >30-40 Myr between the post-collisional  
558 magmatism and HP-UHP metamorphism in typical collisional orogenic belts  
559 worldwide (e.g., Song et al., 2015b). However, the time lag between the  
560 post-collisional magmatism and UHP metamorphism in the EKO is relatively short  
561 and less than 36 Myr, which is different from the typical collisional orogenic belts  
562 around the world. These pieces of evidence indicate that the EKO is distinctive.  
563 Several studies have documented that the seafloor spreading of the Paleo-Tethys  
564 Ocean started at ~383-333 Ma in the northern and eastern Tibetan plateau, with data  
565 from regions such as Qiangtang, East Kunlun, Jinshajiang and Ailaoshan (e.g., Jian et  
566 al., 2009; Zhai et al., 2013; Pei et al., 2018). It is generally accepted that early  
567 continental rifting related to the opening of the Paleo-Tethys Ocean occurred at  
568 ~443-401 Ma, based on low-Ti-CFB xenoliths in the Jinshajiang mélangé (Jian et al.,

569 [2009](#)). This age is almost synchronous with the formation of the post-collisional  
570 igneous rocks (~426-390 Ma) in the EKO. Therefore, we propose that the ~426-390  
571 Ma post-collisional igneous rocks in the EKO are a magmatic response to the early  
572 continental rifting related to the formation of the Paleo-Tethys Ocean.

573 Previous studies have proposed that mantle plumes or back-arc rifting plays a  
574 vital role in the opening of ocean basins (e.g., [Stampfli and Borel, 2002](#); [Zhang et al.,](#)  
575 [2018](#)). In the case of the EKO, back-arc rifting could be responsible for the formation  
576 of the Paleo-Tethys Ocean, because: (1) the large-scale alkaline flood basalts are  
577 absent in the EKO; (2) the calculated mantle/crystallization temperatures for the Tatu  
578 mafic igneous rocks are relatively low (1100-1400 °C; see above), implying that the  
579 EKO did not possess thermal anomalies at this time ([Li et al., 2008b](#); [Lee et al., 2009](#));  
580 and (3) arc-related igneous rocks, dated at ~480-438 Ma ([Liu et al., 2013](#); [Jiang et al.,](#)  
581 [2015](#); [Dong et al., 2018](#)), are common in the EKO. Given the distribution of Early  
582 Paleozoic arc rocks and results of structural analyses ([Liu et al., 2013](#); [Jiang et al.,](#)  
583 [2015](#); [Li et al., 2018](#); [Dong et al., 2018a](#)), we further suggest that the back-arc rifting  
584 could have result from the southwards subduction of the Proto-Tethys Ocean. These  
585 pieces of evidence indicate that the ~426-390 Ma post-collisional igneous rocks in the  
586 EKO recorded the transition from the Proto- to Paleo-Tethys oceans.

587 We propose the following geodynamic model for the full evolution of the EKO  
588 ([Fig. 12](#)). During the Proto-Tethys subduction stage, the lithospheric mantle was  
589 metasomatized by the slab-derived fluids, accompanying the formation of arc-related  
590 igneous rocks (e.g., [Jiang et al., 2015](#); [Dong et al., 2018a](#)), and subduction beneath the

591 East Kunlun-North Qiangtang Block led to back-arc rifting (Fig. 12A). As the  
592 subduction proceeded, the Proto-Tethys oceanic slab reached up to UHP eclogite  
593 facies during ~428-426 Ma (Song et al., 2018), marking the final closure of the  
594 Proto-Tethys Ocean and onset of continental collision (Fig. 12B). Slab break-off of  
595 the Proto-Tethys oceanic plate occurred at ~423 Ma, shortly after continental collision  
596 (Fig. 12B). During this stage, uprising asthenosphere would have impinged upon the  
597 lithospheric mantle of the overriding slab, accompanying exhumation of HP-UHP  
598 rocks and rapid orogenic uplift (Fig. 12B), which is evidenced by the 423-400 Ma  
599 deposition of molasse sediments in the EKO (Lu et al., 2010). In addition, conductive  
600 heating would have resulted in the partial melting of continental crust, generating  
601 426-418 Ma A<sub>2</sub>-type granitoids (Xin et al., 2018; Chen et al., 2020) (Fig. 12B). Finally,  
602 the EKO collapsed by the repeated and localized delamination of the lower  
603 lithosphere during ~412-390 Ma, which could be facilitated by the continental rifting.  
604 The Paleo-Tethys Ocean has started to grow since ~383 Ma (Fig. 12C). During this  
605 process, upwelling of asthenosphere led to the formation of mafic igneous rocks,  
606 which show within-plate geochemical features and have no clear patterns in time and  
607 space (e.g., Yang et al., 2014; Xiong et al., 2014; Zhong et al., 2017).

## 608 **7. Conclusions**

609 The Tatuó mafic igneous rocks are mainly composed of basaltic lavas and  
610 diabase dykes. Geochemical and isotopic data suggest that the basaltic lavas could be  
611 originated from melting of a spinel-bearing asthenosphere (E-MORB) with  
612 insignificant (<4%) crustal contamination, whereas the diabase dykes were likely

613 derived from a spinel-bearing lithospheric mantle metasomatized by slab-derived  
614 fluids with 5-20% crustal contamination. The geochemical features of the Tatuó mafic  
615 igneous rocks are similar to those of within-plate basalts. Magmatic zircons indicate  
616 that the basaltic lavas and diabase dykes formed at  $407.0 \pm 3.9$  Ma and  $402.7 \pm 4.8$   
617 Ma, respectively. The formation of the Tatuó mafic igneous rocks were related to both  
618 the final collapse of the Proto-Tethys orogenic belt, induced by repeated and localized  
619 delamination of lithospheric mantle, and continental rifting related to the formation of  
620 the Paleo-Tethys Ocean.

## 621 **Acknowledgements**

622 We thank Lebing Fu, two anonymous reviewers and Editor-in-chief Xian-Hua Li  
623 for their detailed and constructive comments, which greatly improved the quality of  
624 the paper. We thank the members of the Element Geochemical Lab, China University  
625 of Geosciences, Beijing (CUGB), for their help with major and trace element analyses;  
626 Xiaoli Li for his help with electron probe analyses; Mengqi Jin for her help with  
627 zircon LA-ICP-MS U-Pb dating; Wenping Zhu and Guibing Zhang for their help with  
628 whole-rock Sr-Nd isotopic analyses. We are also grateful to Liming Yang, Hengzhe Bi  
629 and Fan He for their field assistance. This work was financially supported by the  
630 National Natural Science Foundation of China (grants 91955202, 41572040).

## 631 **References**

632 Andersen, T., 2002. [Correction of common lead in U-Pb analyses that do not report](#)  
633 [<sup>204</sup>Pb](#). *Chemical Geology* 192, 59–79.

634 Bi, H.Z., Song, S.G., Dong, J.L., Yang, L.M., Qi, S.S., Allen, M.B., 2018. [First](#)



635 discovery of coesite in eclogite from East Kunlun, northwest China. *Science*  
636 *Bulletin*, 63: 1536–1538.

637 Bian, Q.T., Li, D.H., Pospelov, I., Yin, L.M., Li, H.S., Zhao, D.S., Chang, C.F., Luo,  
638 X.Q., Gao, S.L., Astrakhtantsev, O., Chamov, N., 2004. Age, geochemistry and  
639 tectonic setting of Buqingshan ophiolites, North Qinghai-Tibet Plateau, China.  
640 *Journal of Asian Earth Sciences* 23, 577–596.

641 Bird, P., 1979. Continental delamination and the Colorado Plateau. *Journal of*  
642 *Geophysical Research: Solid Earth* 84, 7561–7571.

643 Bureau of Geology, Qinghai Province (BGQP), 1973. *Geological Map of Jialuhe,*  
644 *Qinghai Province, Scale 1: 200,000 (in Chinese).*

645 Chen, J.J., Fu, L.B., Wei, J.H., Selby, D., Zhang, D.H., Zhou, H.Z., Zhao, X., Liu, Y.,  
646 2020. Proto-Tethys magmatic evolution along northern Gondwana: Insights from  
647 Late Silurian-Middle Devonian A-type magmatism, East Kunlun Orogen,  
648 Northern Tibetan Plateau, China. *Lithos* 356–357, 105304.

649 Chen, J.J., Wei, J.H., Fu, L.B., Li, H., Zhou, H.Z., Zhao, X., Zhan, X.F., Tan, J., 2017.  
650 Multiple sources of the early Mesozoic Gouli batholith, Eastern Kunlun  
651 Orogenic Belt, northern Tibetan Plateau: linking continental crustal growth with  
652 oceanic subduction. *Lithos* 292–293, 161–178.

653 Dong, J.L., Song, S.G., Su, L., Li, Y.G., Yang, L.M., Wang, C., Xu, B., 2019. Onset of  
654 the North-South Gravity Lineament, NE China: constraints of late Jurassic  
655 bimodal volcanic rocks. *Lithos* 334–335, 58–68.

656 Dong, Y.P., He, D.F., Sun, S.S., Liu, X.M., Zhou, X.H., Zhang, F.F., Yang, Z., Cheng,

657 B., Zhao, G.C., Li, J.H., 2018a. Subduction and accretionary tectonics of the East  
658 Kunlun Orogen, western segment of the Central China Orogenic System.  
659 Earth-Science Reviews 186, 231–261.

660 Dong, J.L., Song, S.G., Wang, M.M., Allen, M.B., Su, L., Wang, C., Yang, L.M., Xu,  
661 B., 2018b. Alaskan-type Kedanshan intrusion (central Inner Mongolia, China):  
662 Superimposed subduction between the Mongol-Okhotsk and Paleo-Pacific  
663 oceans in the Jurassic. Journal of Asian Earth Sciences 167, 68–81.

664 Ding, L., Yang, D., Cai, F.L., Pullen, A., Kapp, P., Gehrels, G.E., Zhang, L.Y., Zhang,  
665 Q.H., Lai, Q.Z., Yue, Y.H., Shi, R.D., 2013. Provenance analysis of the Mesozoic  
666 Hoh-Xil–Songpan-Ganzi turbidites in northern Tibet: implications for the  
667 tectonic evolution of the eastern Paleo-Tethys Ocean. Tectonics 32, 1–15.

668 Davies, G.F., 2009. Effect of plate bending on the Urey ratio and the thermal  
669 evolution of the mantle. Earth and Planetary Science Letters 287, 513–518.

670 DePaolo, D.J., 1981. A neodymium and strontium isotopic study of the Mesozoic  
671 calcalkaline granitic batholiths of the Sierra-Nevada and Peninsular Ranges,  
672 California. Journal of Geophysical Research 86, 470–488.

673 Frey, F.A., Green, D.H., Roy, S.D., 1978. Integrated models of basalt petrogenesis: a  
674 study of quartz tholeiites to olivine melilitites from South Eastern Australia  
675 utilizing geochemical and experimental petrological data. Journal of Petrology  
676 19, 463–513.

677 Green, N.L., 2006. Influence of slab thermal structure on basalt source regions and  
678 melting conditions: REE and HFSE constraints from the Garibaldi volcanic belt,

679 northern Cascadia subduction system. *Lithos* 87, 23–49.

680 George, R., Turner, S., Hawkesworth, C., Morris, J., Nye, C., Ryan, J., Zheng, S.-H.,  
681 2003. Melting processes and fluid and sediment transport rates along the Alaska–  
682 Aleutian arc from an integrated U-Th-Ra-Be isotope study. *Journal of*  
683 *Geophysical Research*. doi:10.1029/2002JB001916.

684 George, R., Rogers, N., 2002. Plume dynamics beneath the African plate inferred  
685 from the geochemistry of the Tertiary basalts of southern Ethiopia. *Contributions*  
686 *to Mineralogy and Petrology* 144, 286–304.

687 He, D.F., Dong, Y.P., Liu, X.M., Yang, Z., Sun, S.S., Cheng, B., Li, W., 2016.  
688 Tectono-thermal events in East Kunlun, Northern Tibetan Plateau: evidence from  
689 zircon U-Pb geochronology. *Gondwana Research* 30, 179–190.

690 Hofmann, A., 1997. Mantle geochemistry: the message from oceanic volcanism.  
691 *Nature* 389, 219–229.

692 Houseman, G., McKenzie, D., Molnar, P., 1981. Convective instability of a thickened  
693 boundary layer and its relevance for the thermal evolution of continental  
694 convergent belts. *Journal of Geophysical Research* 86, 6115–6132.

695 Jiang, C.Y., Ling, J.L., Zhou, W., Du, W., Wang, Z.X., Fan, Y.Z., Song, Y.F., Song,  
696 Z.B., 2015. Petrogenesis of the Xiarihamu Ni bearing layered mafic-ultramafic  
697 intrusion, East Kunlun: implications for its extensional island arc environment.  
698 *Acta Petrologica Sinica* 31(4), 1117–1136 (in Chinese with English abstract).

699 Jian, P., Liu, D.Y., Kröner, A., Zhang, Q., Wang, Y.Z., Sun, X.M., Zhang, W., 2009.  
700 Devonian to Permian plate tectonic cycle of the Paleo-Tethys Orogen in

701 southwest China (II): insights from zircon ages of ophiolites, arc/back-arc  
702 assemblages and withinplate igneous rocks and generation of the Emeishan CFB  
703 province. *Lithos* 113, 767–784.

704 Kaislaniemi, L., van Hunen, J., Allen, M.B., Neill, I., 2014. Sublithospheric  
705 small-scale convection—A mechanism for collision zone magmatism. *Geology*  
706 42, 291–294.

707 Kheirkhah, M., Neill, I., Allen, M.B., 2015. Petrogenesis of OIB-like basaltic volcanic  
708 rocks in a continental collision zone: Late Cenozoic magmatism of Eastern Iran.  
709 *Journal of Asian Earth Sciences* 106, 19–33.

710 Lee, C.T.A., Luffi, P., Plank, T., Dalton, H., Leeman, W.P., 2009. Constraints on the  
711 depths and temperatures of basaltic magma generation on Earth and other  
712 terrestrial planets using new thermobarometers for mafic magmas. *Earth and*  
713 *Planetary Science Letters* 279, 20–33.

714 Li, S.Z., Zhao, S.J., Liu, X., Cao, H., Yu, S., Li, X.Y., Somerville, I., Yu, S.Y., 2018.  
715 Closure of the Proto-Tethys Ocean and Early Paleozoic amalgamation of  
716 microcontinental blocks in East Asia. *Earth-Science Reviews* 186, 37–75.

717 Liu, B., Ma, C.Q., Jiang, H.A., Guo, P., Zhang, J.Y., Xiong, F.H., 2013. Early  
718 Paleozoic tectonic transition from ocean subduction to collisional orogeny in the  
719 Eastern Kunlun region: Evidence from Huxiaoqin mafic rocks. *Acta Petrologica*  
720 *Sinica* 29, 2093–2106 (in Chinese with English abstract).

721 Li, Z.X., Bogdanova, S.V., Collins, A.S., Davidson, A., DeWaele, B., Ernst, R.E.,  
722 Fitzsimons, I.C.W., Fuck, R.A., Gladkochub, D.P., Jacobs, J., Karlstrom, K.E.,

723 Lu, S., Natapov, L.M., Pease, V., Pisarevsky, S.A., Thrane, K., Vernikovsky, V.,  
724 2008a. [Assembly, configuration, and break-up history of Rodinia: a synthesis.](#)  
725 [Precambrian Research](#) 160, 179–210.

726 Li, X.H., Li, W.X., Li, Z.X., Liu, Y., 2008b. [850-790 Ma bimodal volcanic and](#)  
727 [intrusive rocks in northern Zhejiang, South China: a major episode of continental](#)  
728 [rift magmatism during the breakup of Rodinia.](#) *Lithos* 102, 341–357.

729 Lu, L., Wu, Z.H., Hu, D.G., Barosh. P.J., Hao, S., Zhou, C.J., 2010. [Zircon U-Pb age](#)  
730 [for rhyolite of the Maoniushan Formation and its tectonic significance in the East](#)  
731 [Kunlun Mountains.](#) *Acta Petrologica Sinica* 26 (4), 1150–1158 (in Chinese with  
732 [English abstract](#)).

733 Ludwig, K.R., 2003. [User's manual for Isoplot 3.00: a geochronological toolkit for](#)  
734 [Microsoft Excel \(No. 4\).](#) Kenneth R. Ludwig.

735 Metcalfe, I., 2013. [Gondwana dispersion and Asian accretion: Tectonic and](#)  
736 [palaeogeographic evolution of eastern Tethys.](#) *Journal of Asian Earth Sciences* 66,  
737 1–33.

738 Morency, C., Doin, M.-P., Dumoulin, C., 2002. [Convective destabilization of a](#)  
739 [thickened continental lithosphere.](#) *Earth and Planetary Science Letters* 202,  
740 303–320.

741 Meng, F.C., Zhang, J.X., Cui, M.H., 2013. [Discovery of Early Paleozoic eclogite from](#)  
742 [the East Kunlun, Western China and its tectonic significance.](#) *Gondwana*  
743 [Research](#) 23, 825–836.

744 Muravyeva, N.S., Belyatsky, B.V., Senin, V.G., Ivanov, A.V., 2014. [Sr-Nd-Pb isotope](#)

745 systematics and clinopyroxene-host disequilibrium in ultra-potassic magmas  
746 from Toro-Ankole and Virunga, East-African Rift: Implications for magma  
747 mixing and source heterogeneity. *Lithos* 210–211, 260–277.

748 Macera, P.M., Gasperini, D., Ranalli, G., Mahatsent, R., 2008. Slab detachment and  
749 mantle plume upwelling in subduction zones: an example from the Italian  
750 South-Eastern Alps. *Journal of Geodynamics* 45, 32–48.

751 Melluso, L., Mahoney, J.J., Dallai, L., 2006. Mantle sources and crustal input as  
752 recorded in high-Mg Deccan Traps basalts of Gujarat (India). *Lithos* 89,  
753 259–274.

754 Mühe, R., Bohrmann, H., Garbe-Schönberg, D., Kassens, H., 1997. E-MORB glasses  
755 from the Gakkel Ridge (Arctic Ocean) at 87°N: evidence for the Earth's most  
756 northerly volcanic activity. *Earth and Planetary Sciences Letters* 152 (1), 1–9.

757 Morimoto, N., 1988. Nomenclature of pyroxenes. *Mineralogy and Petrology* 39,  
758 55–76.

759 Miyashiro, A., 1974. Volcanic rock series in island arcs and active continental margins.  
760 *American Journal of Science* 274 (4), 321–355.

761 Nimis, P., Taylor, W.R., 2000. Single clinopyroxene thermobarometry for garnet  
762 peridotites: Part I. Calibration and testing of a Cr-in-Cpx barometer and an  
763 enstatite-in-cpx thermometer. *Contributions to Mineralogy and Petrology* 139,  
764 541–554.

765 Pei, X.Z., Li, R.B., Li, Z.C., Liu, C.J., Chen, Y.X., Pei, L., Liu, Z.Q., Chen, G.C., Li,  
766 X.B., Wang, M., 2018. Composition feature and formation process of

767 Buqingshan composite accretionary mélangé belt in southern margin of East  
768 Kunlun orogen. *Earth Science* 43 (12): 4498–4520 (in Chinese with English  
769 abstract).

770 Pearce, J.A., 2008. Geochemical fingerprinting of oceanic basalts with application to  
771 ophiolite classification and the search for Archean oceanic crust. *Lithos* 100,  
772 14–48.

773 Pearce, J.A., Stern, R.J., Bloomer, S.H., Fryer, P., 2005. Geochemical mapping of the  
774 Mariana arc-basin system: implications for the nature and distribution of  
775 subduction components. *Geochemistry Geophysics Geosystems* 6, Q07006.  
776 <http://dx.doi.org/10.1029/2004GC000895>.

777 Prelević, D., Akal, C., Foley, S.F., Romer, R.L., Stracke, A., Van Den Bogaard, P.,  
778 2012. Ultrapotassic Mafic Rocks as Geochemical Proxies for Post-collisional  
779 Dynamics of Orogenic Lithospheric Mantle: the Case of Southwestern Anatolia,  
780 Turkey. *Journal of Petrology* 53, 1019–1055.

781 Qi, S.S., Song, S.G., Shi, L.C., Cai, H.J., Hu, S.C., 2014. Discovery and its geological  
782 significance of early Paleozoic eclogite in Xiarihamu-Suhaitu area, western part  
783 of the east Kunlun. *Acta Petrologica Sinica* 30, 3345–3356 (in Chinese with  
784 English abstract).

785 Rudnick, R.L., Gao, S., 2003. The composition of the continental crust. In: Rudnick,  
786 R.L. (Ed.), *The Crust*. Elsevier-Pergamon, Oxford, pp. 1–64.

787 Rublee, V.J., 1994. *Chemical Petrology, Mineralogy and Structure of the Tulameen*  
788 *Complex, Princeton Area, British Columbia*. Unpublished M.Sc. Thesis.

789 University of Ottawa, Canada, p. 179.

790 Song, Y.T., Su, L., Dong, J.L., Song, S.G., Allen, M.B., Wang, C., Hu, X.L., 2020.

791 Detrital zircons from Late Paleozoic to Triassic sedimentary rocks of the

792 Gongshan-Baoshan Block, SE Tibet: Implications for episodic crustal growth of

793 Eastern Gondwana. *Journal of Asian Earth Sciences* 188, 104106.

794 Song, S.G., Bi, H.Z., Qi, S.S., Yang, L.M., Allen, M.B., Niu, Y.L., Su, L., Li, W.F.,

795 2018. HP-UHP metamorphic belt in the East Kunlun orogen: final closure of the

796 Proto-Tethys Ocean and formation of Pan-North-China Continent. *Journal of*

797 *Petrology* 59 (11), 2043–2060.

798 Song, S.G., Yang, L.M., Zhang, Y.Q., Niu, Y.L., Wang, C., Su, L., Gao, Y. L., 2017.

799 Qi-Qin Accretionary Belt in Central China Orogen: accretion by trench jam of

800 oceanic plateau and formation of intra-oceanic arc in the Early Paleozoic

801 Qin-Qi-Kun Ocean. *Science Bulletin* 62, 1035–1038.

802 Song, S.G., Wang, M.M., Xu, X., Wang, C., Niu, Y.L., Allen, M.B., Su, L., 2015a.

803 Ophiolites in the Xing'an-Inner Mongolia accretionary belt of the CAOB:

804 Implications for two cycles of seafloor spreading and accretionary orogenic

805 events. *Tectonics* 34, 2221–2245.

806 Song, S., Wang, M., Wang, C., Niu, Y., 2015b. Magmatism during continental

807 collision, subduction, exhumation and mountain collapse in collisional orogenic

808 belts and continental net growth: A perspective. *Science China Earth Sciences* 58,

809 1284–1304.

810 Stampfli, G.M., Borel, G.D., 2002. A plate tectonic model for the Paleozoic and



811 Mesozoic constrained by dynamic Plate boundaries and restored synthetic  
812 oceanic isochrons. *Earth and Planetary Science Letters* 196 (1–2), 17–33.

813 Sun, S.S., McDonough, W.F., 1989. Chemical and isotopic systematics of oceanic  
814 basalts: implications for mantle composition and processes. Geological Society  
815 of London, Special Publication 42, 313–345.

816 Smith, J.V., Brown, W.L., 1988. *Feldspar Minerals: Second Revised and Extended*  
817 *Edition*. Springer Verlag, Berlin Heidelberg, New York, London, Paris, Tokyo.

818 Shervais, J.W., 1982. Ti-V plots and the petrogenesis of modern and ophiolitic lavas.  
819 *Earth and Planetary Science Letters* 59, 101–118.

820 Tian, G.K., Meng, F.C., Fan, Y.Z., Liu, Q., Duan, X.P., 2016. The characteristics of  
821 early Paleozoic post-orogenic granite in the east Kunlun orogen: a case study of  
822 Dagangou granite. *Acta Petrologica et Mineralogica* 35, 371–390 (in Chinese  
823 with English abstract).

824 von Raumer, J.F., Stampfli, G.M., 2008. The birth of the Rheic Ocean-Early  
825 Palaeozoic subsidence patterns and subsequent tectonic plate scenarios.  
826 *Tectonophysics* 461 (1-4), 9–20.

827 von Blanckenburg, F., Davies, J.H., 1995. Slab break off: a model for syncollisional  
828 magmatism and tectonics in the Alps. *Tectonics* 14 (1), 120–131.

829 Wan, Y., Zhang, J., Yang, J., Xu, Z., 2006. Geochemistry of high-grade metamorphic  
830 rocks of the North Qaidam mountains and their geological significance. *Journal*  
831 *of Asian Earth Sciences* 28, 174–184.

832 Wilson, M., 1989. *Igneous Petrogenesis*. Unwin Hyman, London.

833 Winchester, J.A., Floyd, P.A., 1976. [Geochemical magma type discrimination:](#)  
834 [application to altered and metamorphosed basic igneous rocks.](#) *Earth and*  
835 [Planetary Science Letters](#) 28, 459–469.

836 Xia, W.C., Zhang, N., Yuan, X.P., Fan, L.S., Zhang, B.S., 2001. [Cenozoic Qaidam](#)  
837 [basin, China: a stronger tectonic inverted, extensional rifted basin.](#) *AAPG Bull.*  
838 [85, 715–736.](#)

839 Xiong, F., Ma, C., Jiang, H.a., Liu, B., Huang, J., 2014. [Geochronology and](#)  
840 [geochemistry of Middle Devonian mafic dykes in the East Kunlun orogenic belt,](#)  
841 [Northern Tibet Plateau: Implications for the transition from Prototethys to](#)  
842 [Paleotethys orogeny.](#) *Chemie der Erde-Geochemistry* 74, 225–235.

843 Xin, W., Sun, F.Y., Li, L., Yan, J.M., Zhang, Y.T., Wang, Y.C., Shen, TS., Yang, Y.J.,  
844 2018. [The Wulonggou metaluminous A<sub>2</sub>-type granites in the Eastern Kunlun](#)  
845 [Orogenic Belt, NW China: Rejuvenation of subduction-related felsic crust and](#)  
846 [implications for post-collision extension.](#) *Lithos* 312–313, 108–127.

847 Yang, L., Zhou, H.W., Zhu, Y.H., Dai, X., Lin, Q.X., Ma, Z.Q., Jian, K.K., Zhang,  
848 M.Y., 2014. [Geochemical characteristics and LA-ICP-MS zircon U-Pb ages of](#)  
849 [intermediate to mafic dyke swarms in Haxiya area, Golmud, Qinghai Province.](#)  
850 [Geological Bulletin of China](#) 33, 804–819 (in Chinese with English abstract).

851 Yang, J.S., Robinson, P.T., Jiang, C.F., Xu, Z.Q., 1996. [Ophiolites of the Kunlun](#)  
852 [mountains, China and their tectonic implications.](#) *Tectonophysics* 258, 215–231.

853 Yuan, C., Zhou, M.F., Sun, M., Zhao, Y.J., Wilde, S., Long, X.P., Yan, D.P., 2010.  
854 [Triassic granitoids in the eastern Songpan Ganzi Fold Belt, SW China: magmatic](#)

855 response to geodynamics of the deep lithosphere. *Earth and Planetary Science*  
856 *Letters* 290, 481–492.

857 Zhao, G.C., Wang, Y.J., Huang, B.C., Dong, Y.P., Li, S.Z., Zhang, G.W., Yu, S., 2018a.  
858 Geological reconstructions of the East Asian blocks: From the breakup of  
859 Rodinia to the assembly of Pangea. *Earth-Science Reviews* 186, 262–286.

860 Zhao, Z., Wei, J., Santosh, M., Liang, S., Fu, L., Zhao, S., Li, H., 2018b. Late  
861 Devonian postcollisional magmatism in the ultrahigh- pressure metamorphic belt,  
862 Xitieshan terrane, NW China. *Geological Society of America Bulletin* 130,  
863 999–1016.

864 Zhao, Z., Wei, J., Fu, L., Liang, S., Zhao, S., 2017. The Early Paleozoic Xitieshan  
865 syn-collisional granite in the North Qaidam ultrahigh-pressure metamorphic belt,  
866 NW China: Petrogenesis and implications for continental crust growth. *Lithos*  
867 278–281, 140–152.

868 Zhang, G.L., Luo, Q., Zhao, J., Jackson, M.G., Guo, L.S., Zhong, L.F., 2018.  
869 Geochemical nature of sub-ridge mantle and opening dynamics of the South  
870 China Sea. *Earth and Planetary Science Letters* 489, 145–155.

871 Zhang, J., Ma, C., Xiong, F., Liu, B., Li, J., Pan, Y., 2014. Early Paleozoic high-Mg  
872 diorite-granodiorite in the eastern Kunlun Orogen, western China: Response to  
873 continental collision and slab break-off. *Lithos* 210–211, 129–146.

874 Zhai, Q.G., Jahn, B.M., Wang, J., Su, L., Mo, X.-X., Wang, K.-L., Tang, S.-H., Lee,  
875 H.-Y., 2013. The Carboniferous ophiolite in the middle of the Qiangtang terrane,  
876 Northern Tibet: SHRIMP U-Pb dating, geochemical and Sr-Nd-Hf isotopic

877 characteristics. *Lithos* 168-169, 186–199.

878 Zhai, Q.G., Zhang, R.Y., Jahn, B.M., Li, C., Song, S.G., Wang, J., 2011. [Triassic](#)  
879 [eclogites from central Qiangtang, northern Tibet, China: petrology,](#)  
880 [geochronology and metamorphic P-T path.](#) *Lithos* 125 (1–2), 173–189.

881 Zhao, J.-H., Zhou, M.-F., 2007. [Geochemistry of Neoproterozoic mafic intrusions in](#)  
882 [the Panzhihua district \(Sichuan Province, SW China\): implications for](#)  
883 [subduction-related metasomatism in the upper mantle.](#) *Precambrian Research*  
884 [152, 27–47.](#)

885 Zheng, Z., Chen, Y.J., Deng, X.H., Yue, S.W., Chen, H.J., Wang, Q.F., 2018. [Origin of](#)  
886 [the Bashierxi monzogranite, Qimantagh, East Kunlun Orogen, NW China: a](#)  
887 [magmatic response to the evolution of the Proto-Tethys Ocean.](#) *Lithos* 296-299,  
888 [181–194.](#)

889 Zhong, S., Feng, C., Seltnann, R., Li, D., 2017. [Middle Devonian volcanic rocks in](#)  
890 [the Weibao Cu-Pb-Zn deposit, East Kunlun Mountains, NW China: Zircon](#)  
891 [chronology and tectonic implications.](#) *Ore Geology Reviews* 84, 309–327.

892 Zhu, D.C., Wang, Q., Zhao, Z.D., Chung, S.L., Cawood, P.A., Niu, Y.L., Liu, S.A.,  
893 [Wu, F.Y., Mo, X.X., 2015. Magmatic record of India–Asia collision.](#) *Scientific*  
894 [Reports](#) 5, 14289.

895 Zhu, W.-G., Zhong, H., Li, X.-H., Deng, H.-L., He, D.-F., Wu, K.-W., Bai, Z.-J., 2008.  
896 [SHRIMP zircon U-Pb geochronology, elemental, and Nd isotopic geochemistry](#)  
897 [of the Neoproterozoic mafic dykes in the Yanbian area, SW China.](#) *Precambrian*  
898 [Research](#) 164, 66–85.

899 Zhou, B., Dong, Y., Zhang, F., Yang, Z., Sun, S., He, D., 2016. [Geochemistry and](#)  
900 [zircon U-Pb geochronology of granitoids in the East Kunlun Orogenic Belt,](#)  
901 [northern Tibetan Plateau: origin and tectonic implications.](#) *Journal of Asian Earth*  
902 [Sciences](#) 130, 265–281.

903 Zhou, J.B., Li, X.-H., Ge, W.C., Li, Z.-X., 2007. [Age and origin of middle](#)  
904 [Neoproterozoic mafic magmatism in southern Yangtze Block and relevance to](#)  
905 [the break-up of Rodinia.](#) *Gondwana Research* 12, 184–197.

906 **Figure Captions**

907

908 **Fig. 1.** (A) Sketch map showing major tectonic units of mainland China, showing the location of  
909 East Kunlun in northwest China, modified after [Song et al. \(2017\)](#). (B) Simplified geological map  
910 of the East Kunlun Orogen and Qaidam-Qilian Orogenic Belt modified after [Song et al. \(2018\)](#).  
911 CAOB = Central Asian Orogenic Belt, CCOB = Central China Orogenic Belt, NCC = North China  
912 Craton, SCC = South China Craton, TB = Tarim Block, QT = Qiangtang Block, SU = Sibumasu  
913 block, NQAB = North Qilian Accretionary Belt, SQAB = South Qilian Accretionary Belt, NQUB  
914 = North Qaidam UHPM Belt.

915

916 **Fig. 2.** (A) Geological map of the Tatuó area, modified after [BGQP \(1973\)](#). (B) Stratigraphic  
917 columns from the Kehete-Tatuó area, mainly showing the Silurian-Devonian volcanic-sedimentary  
918 strata. Pre. = Precambrian, Me. = Mesozoic.

919

920 **Fig. 3.** Field and photomicrographs of the Tatu mafic igneous rocks. (A) and (B) Field  
921 occurrence of basaltic lavas. (C) and (D) Basalts showing phenocrysts in a matrix, composed of  
922 oriented fine- to micro-grained plagioclase, clinopyroxene, opaque mineral and altered minerals  
923 (cross-polarized light). (E) Dolerites showing a fine-grained ophitic texture (cross-polarized light).  
924 (F) and (G) Field occurrence of diabase dykes. (H) and (I) Diabase dykes showing fine- to  
925 medium-grained ophitic textures (cross-polarized light).



926

927 **Fig. 4.** (A) An-Ab-Or triangular diagram ([Smith and Brown, 1988](#)) showing the compositions of  
928 plagioclase for the Tatuio diabase dykes. (B) Wo-En-Fs diagram ([Morimoto, 1988](#)) for  
929 clinopyroxene for the Tatuio diabase dykes. (C) Alz (percentage of tetrahedral sites occupied by Al)  
930 versus TiO<sub>2</sub> (wt.%) diagram for the Tatuio diabase dykes. Tulameen data are from [Rublee \(1994\)](#).  
931 Rift-related Cpx compositions are from [Zhu et al. \(2008\)](#), [Li et al. \(2008b\)](#) and [Muravyeva et al.](#)  
932 [\(2014\)](#).

933

934 **Fig. 5.** (A) Zr/TiO<sub>2</sub> versus Nb/Y ([Winchester and Floyd, 1976](#)), (B) TiO<sub>2</sub> versus FeO<sub>T</sub>/MgO  
935 ([Miyashiro, 1974](#)) and (C) Sm/Yb versus Ti/Y diagrams for the Tatu mafic igneous rocks.

936

937 **Fig. 6.** Chondrite-normalized REE and primitive mantle-normalized multi-element patterns for the  
938 Tatu mafic igneous rocks. Chondrite and primitive mantle normalizing values and N-MORB,  
939 E-MORB and OIB data are after [Sun and McDonough \(1989\)](#). Literature data are from [George et](#)  
940 [al. \(2003\)](#), [Pearce et al. \(2005\)](#) and [Melluso et al. \(2006\)](#).

941

942 **Fig. 7.** CL images of representative zircon grains and concordia diagrams for the Tatuo mafic

943 igneous rocks.

944

945 **Fig. 8.** (A)  $\epsilon_{\text{Nd}}(t)$  versus  $I_{\text{Sr}}(t)$ , and (B)  $\epsilon_{\text{Nd}}(t)$  versus Mg# diagrams for the Tatu mafic igneous

946 rocks.

947

948 **Fig. 9.** Plots of MgO versus SiO<sub>2</sub> (A), FeO<sub>T</sub> versus SiO<sub>2</sub> (B), Al<sub>2</sub>O<sub>3</sub> versus SiO<sub>2</sub> (C), TiO<sub>2</sub> versus  
949 MgO (D), Ni versus Cr (E) and V versus Cr (F) for the Tatu mafic igneous rocks.

950

951 **Fig. 10.** (A) Th/Yb versus Nb/Yb (Pearce, 2008), (B) Nb/Th versus Na/La, (C) Nb/Zr versus  
952 Th/Zr (Zhao and Zhou, 2007) and (D) Th/Nb versus  $\epsilon_{Nd}(t)$  diagrams for the Tatu mafic igneous  
953 rocks. Primitive mantle (PM), N-MORB, E-MORB and OIB data are after Sun and McDonough  
954 (1989). The data for the lower and upper continental crust are from Rudnick and Gao (2003). The  
955 continental crust composition (Th=22.9 ppm, Nb=18.5 ppm and  $\epsilon_{Nd}(t)=-8.06$ ) is represented by the  
956 Wanbaogou sandstone (unpublished data). The SCLM composition (Th=0.08 ppm, Nb=0.12 ppm  
957 and  $\epsilon_{Nd}(t)=-1.39$ ) is from the Xiarihamu mafic-ultramafic intrusion in the EKO and is after Jiang et  
958 al. (2015). The asthenospheric mantle composition (Th=0.44 ppm, Nb=6.35 ppm and  $\epsilon_{Nd}(t)=+7.0$ )  
959 is from the Gakkal Ridge proposed by Mühe et al. (1997). LCC = Lower continental crust. UCC =  
960 Upper continental crust. SCLM = Subcontinental lithospheric mantle.

961

962 **Fig. 11.** (A) Tb/Yb versus La/Yb ([George and Rogers, 2002](#)) and (B) V versus Ti/1000 ([Shervais,](#)  
963 [1982](#)) diagrams for the Tatu mafic igneous rocks. (C) The relative probability density and (D)  
964 zircon  $\epsilon_{\text{Hf}}(t)$  versus Age (Ma) diagrams for the Cambrian to Devonian magmatic rocks in the EKO.  
965 Age and zircon  $\epsilon_{\text{Hf}}(t)$  data are from [Tian et al. \(2016\)](#), [Zhou et al. \(2016\)](#), [Zheng et al. \(2018\)](#), [Xin](#)  
966 [et al. \(2018\)](#) and references therein and [Chen et al. \(2020\)](#).



967

968 **Fig. 12.** Schematic cartoons showing the tectonic evolution of the EKO from the Cambrian to

969 Devonian. QB = Qaidam Block, EKB = East Kunlun Block, NQTB = North Qiangtang Block.

Fig.1-R3  
[Click here to download high resolution image](#)

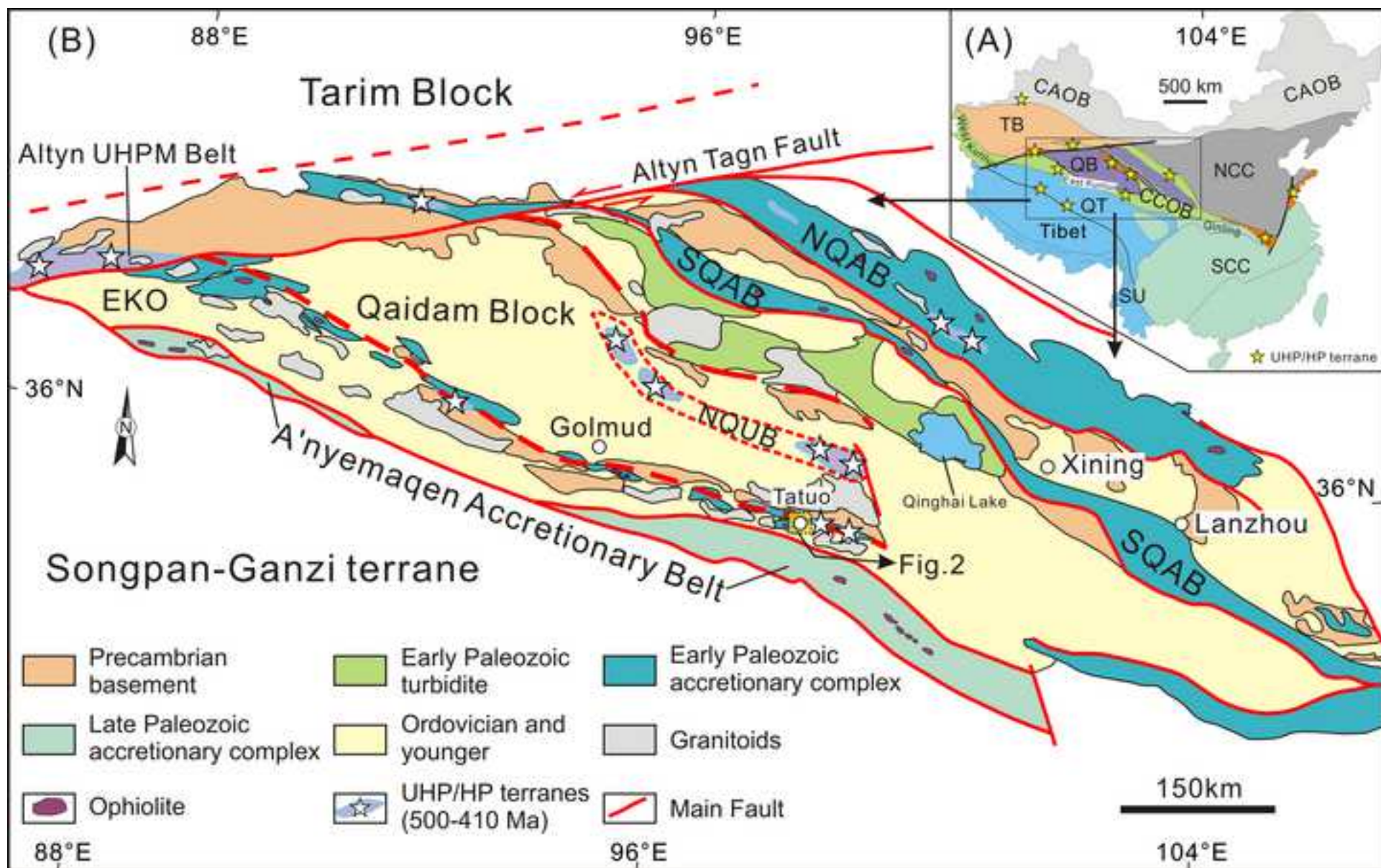


Fig.2-R3

[Click here to download high resolution image](#)

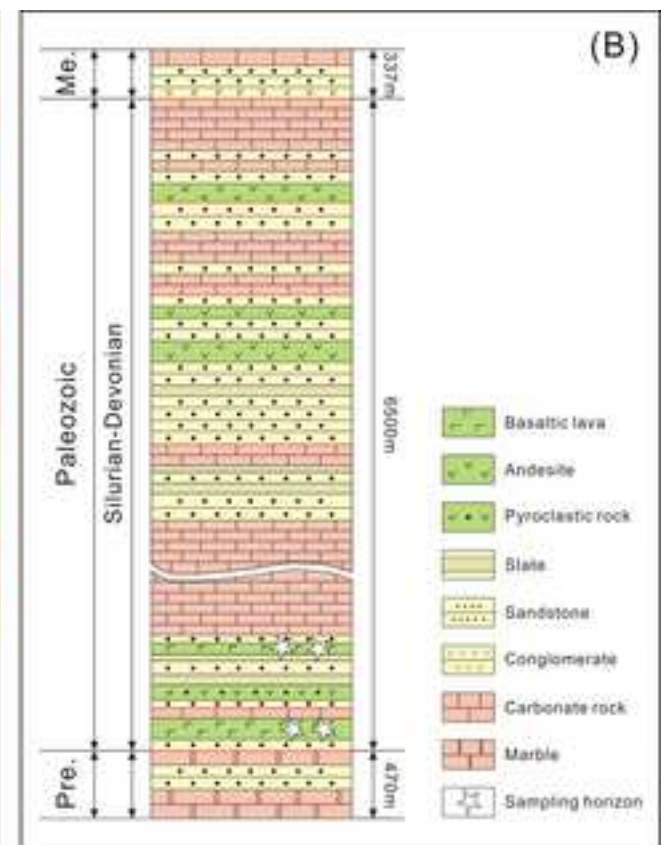
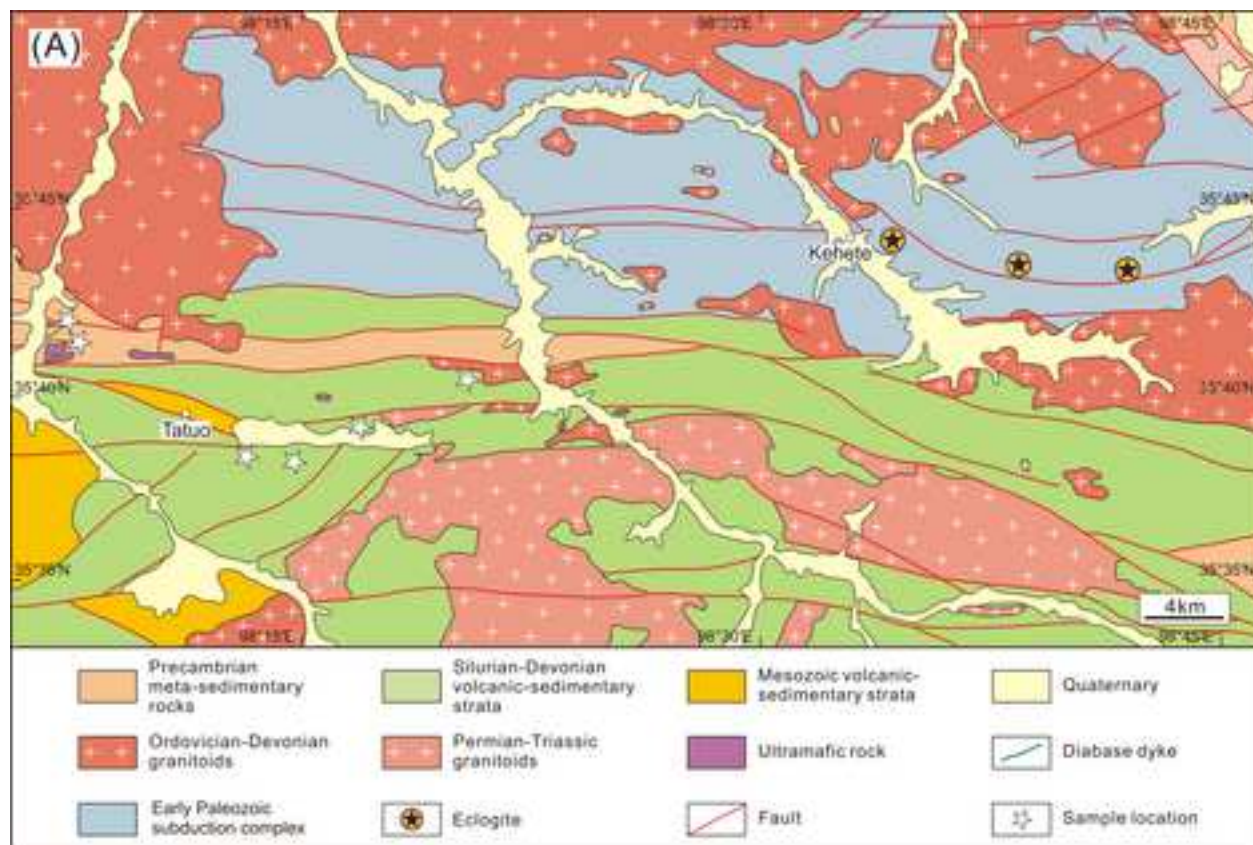


Fig.3-R3  
[Click here to download high resolution image](#)



Fig.4-R3  
[Click here to download high resolution image](#)

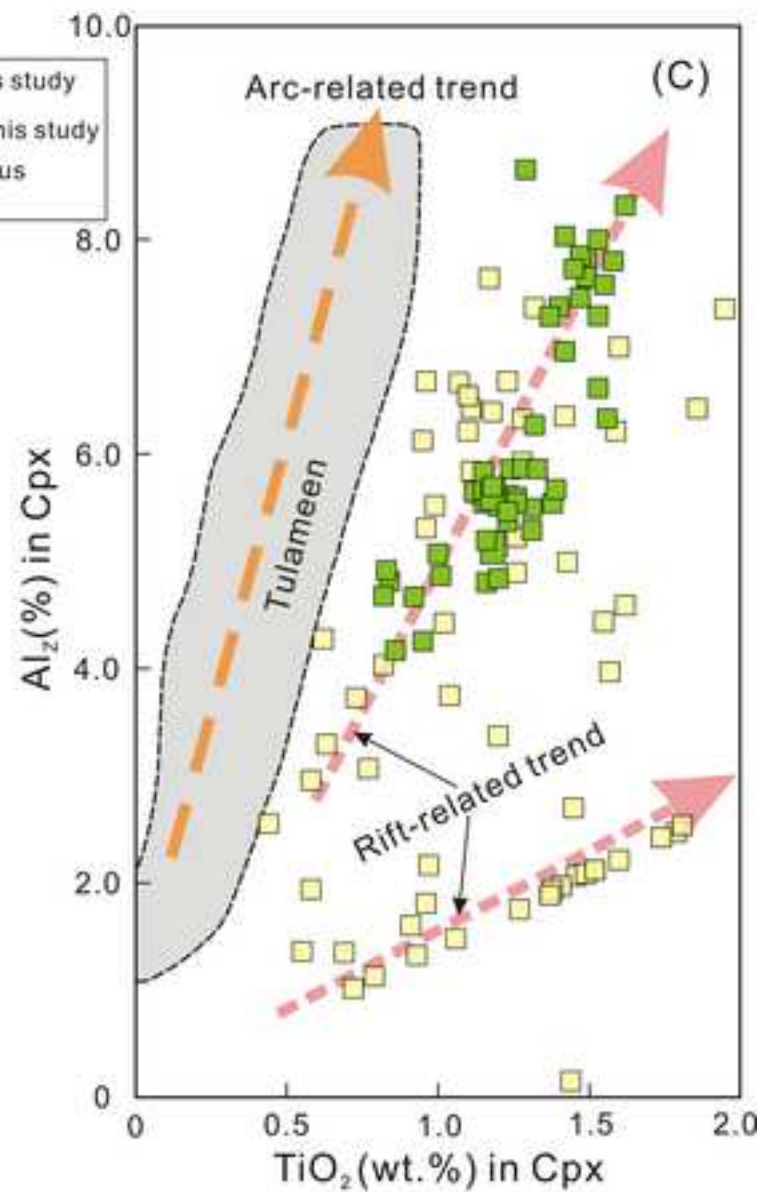
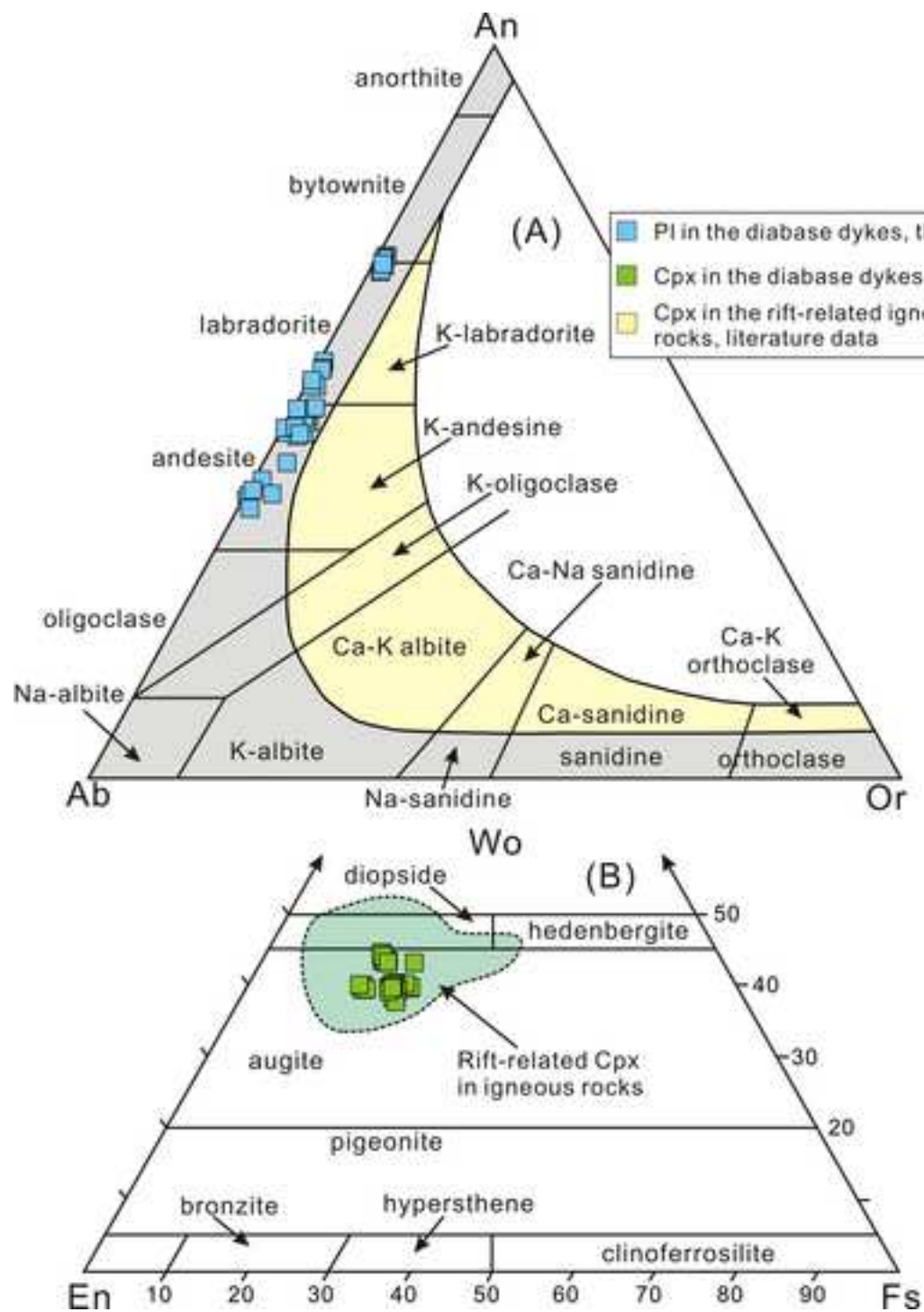


Fig.5-R3

[Click here to download high resolution image](#)

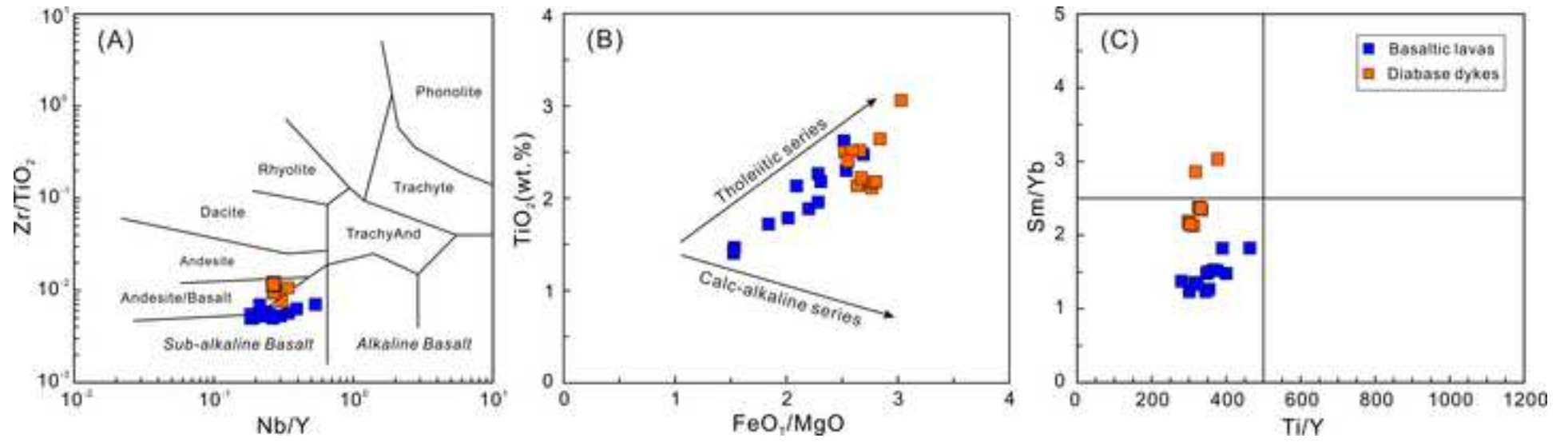


Fig.6-R3  
[Click here to download high resolution image](#)

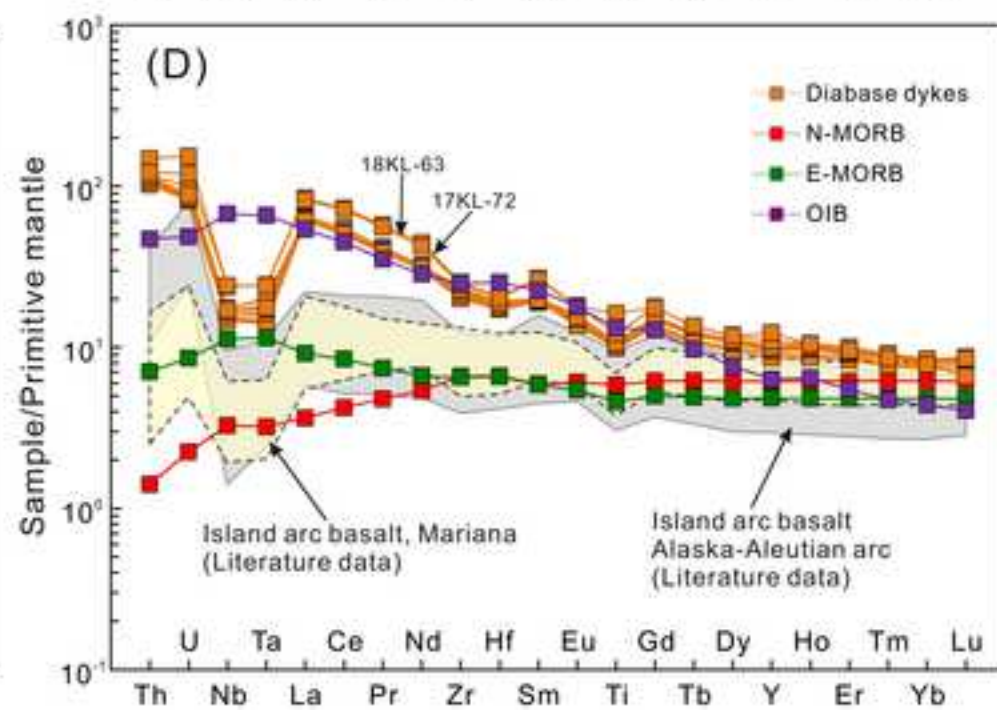
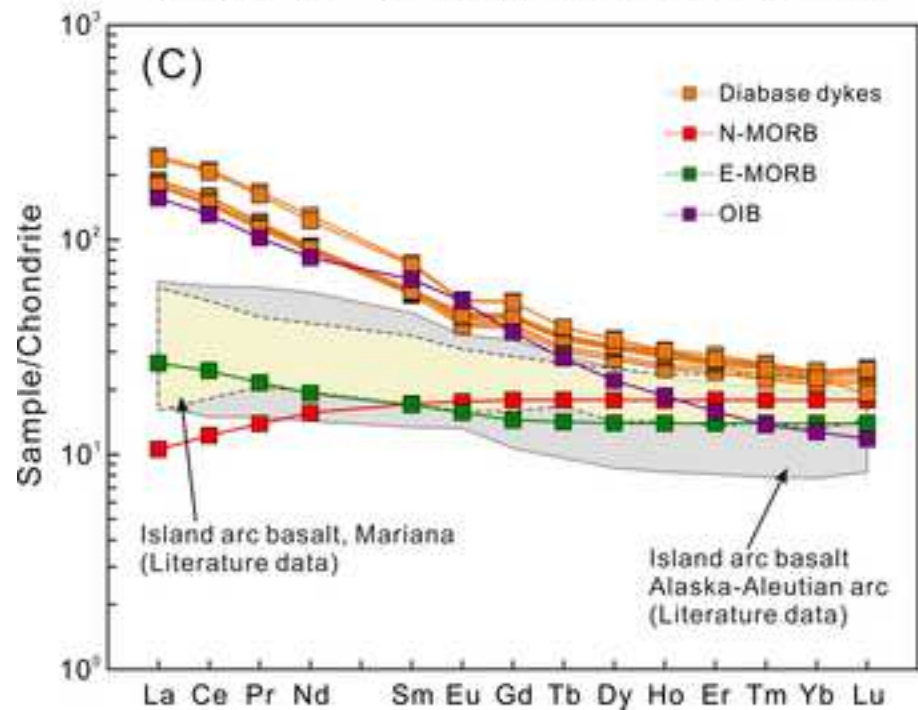
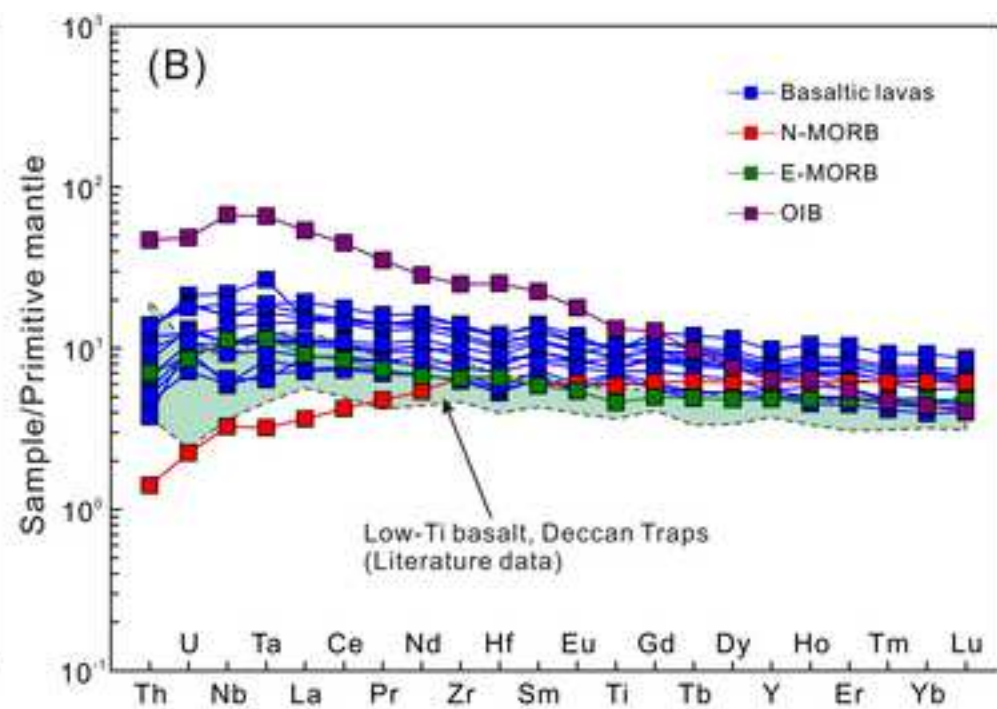
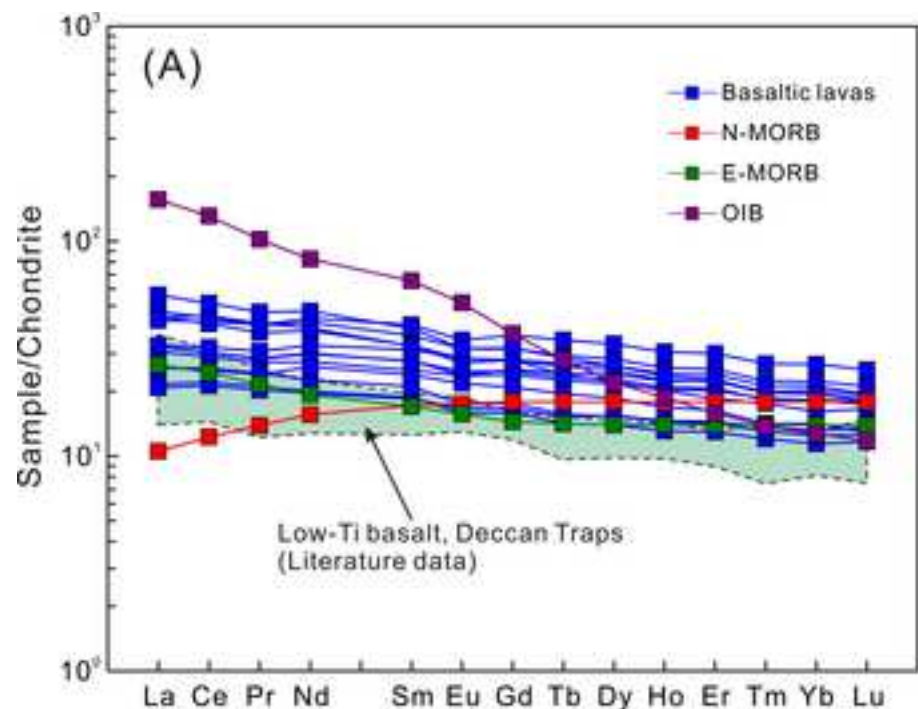


Fig.7-R3  
[Click here to download high resolution image](#)

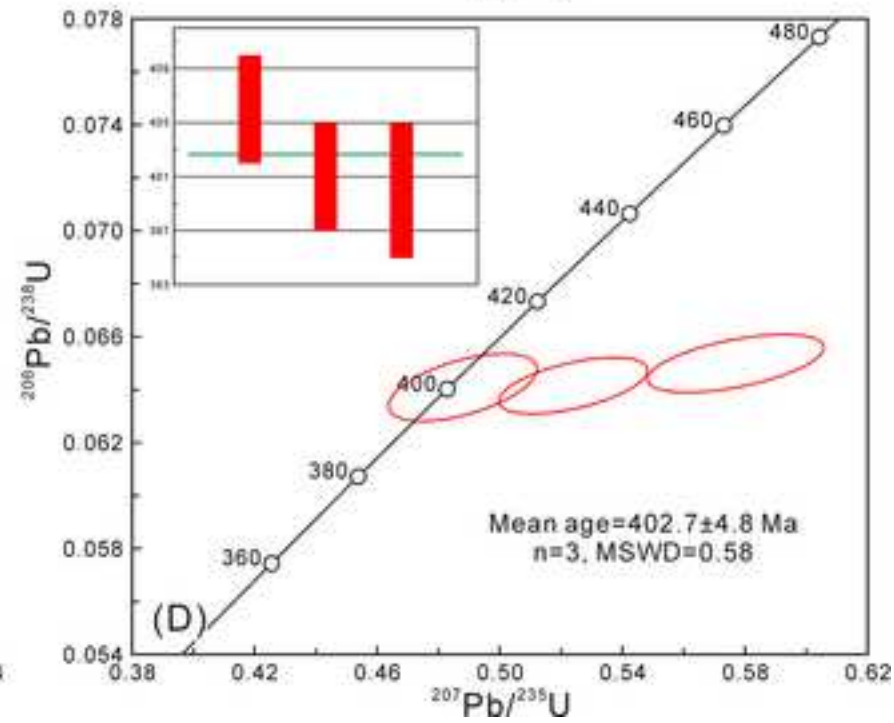
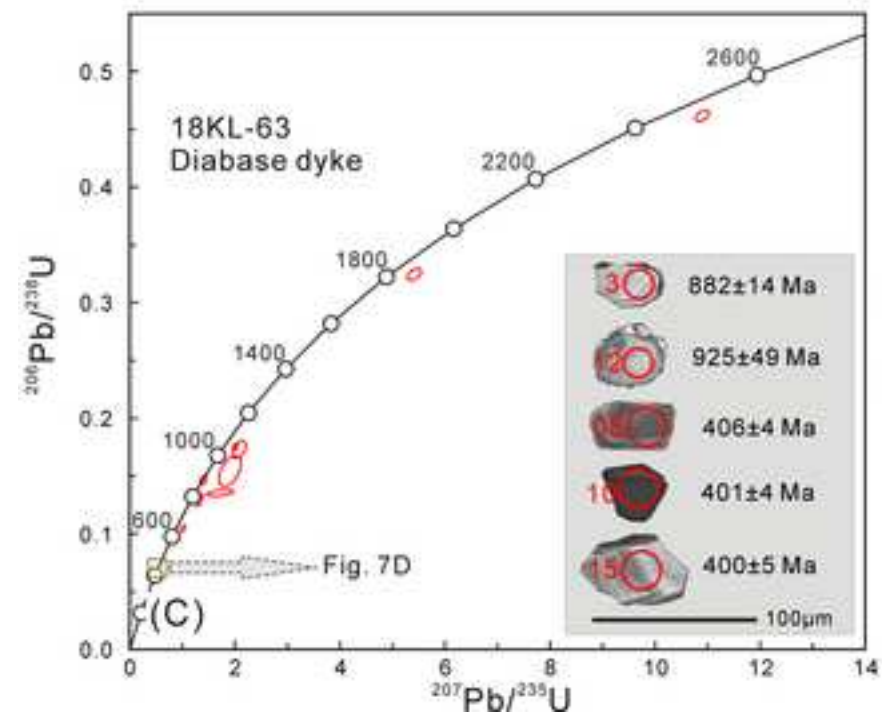
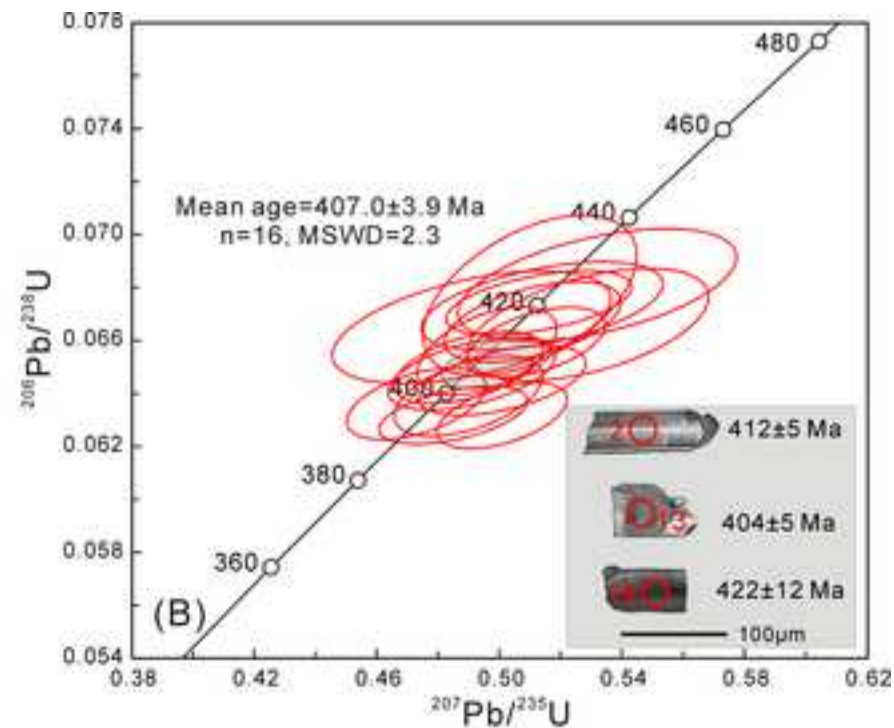
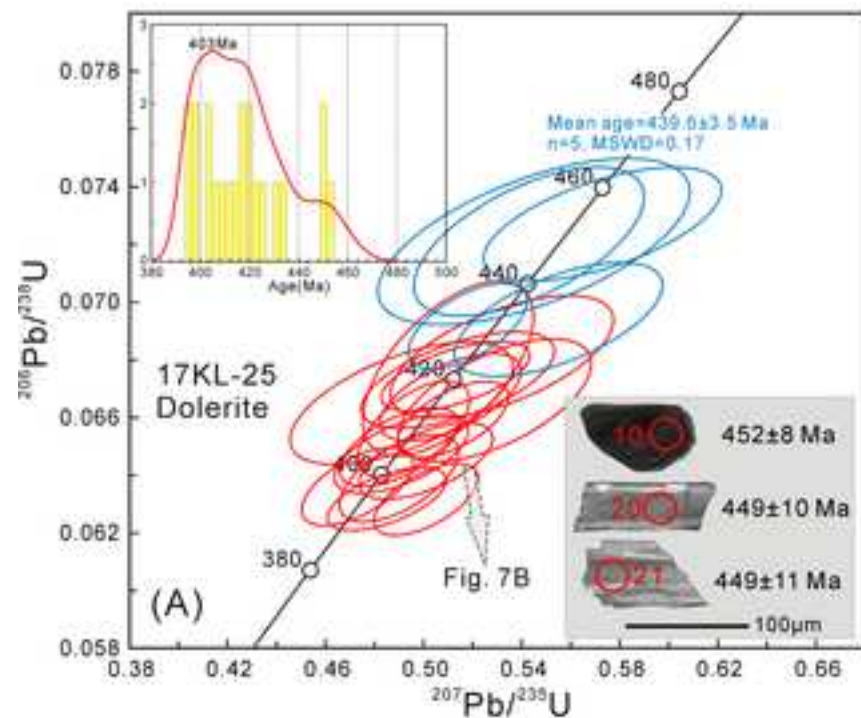




Fig.8-R3  
[Click here to download high resolution image](#)

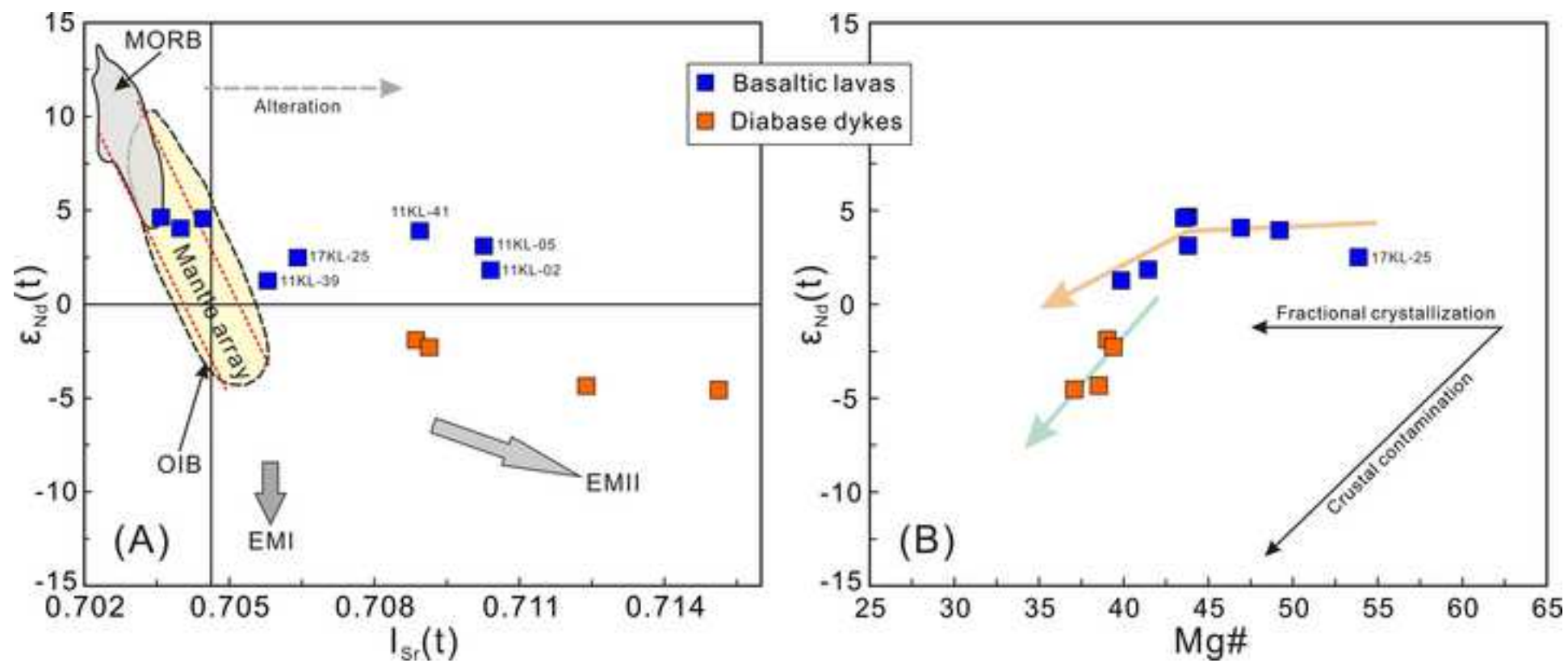


Fig.9-R3  
[Click here to download high resolution image](#)

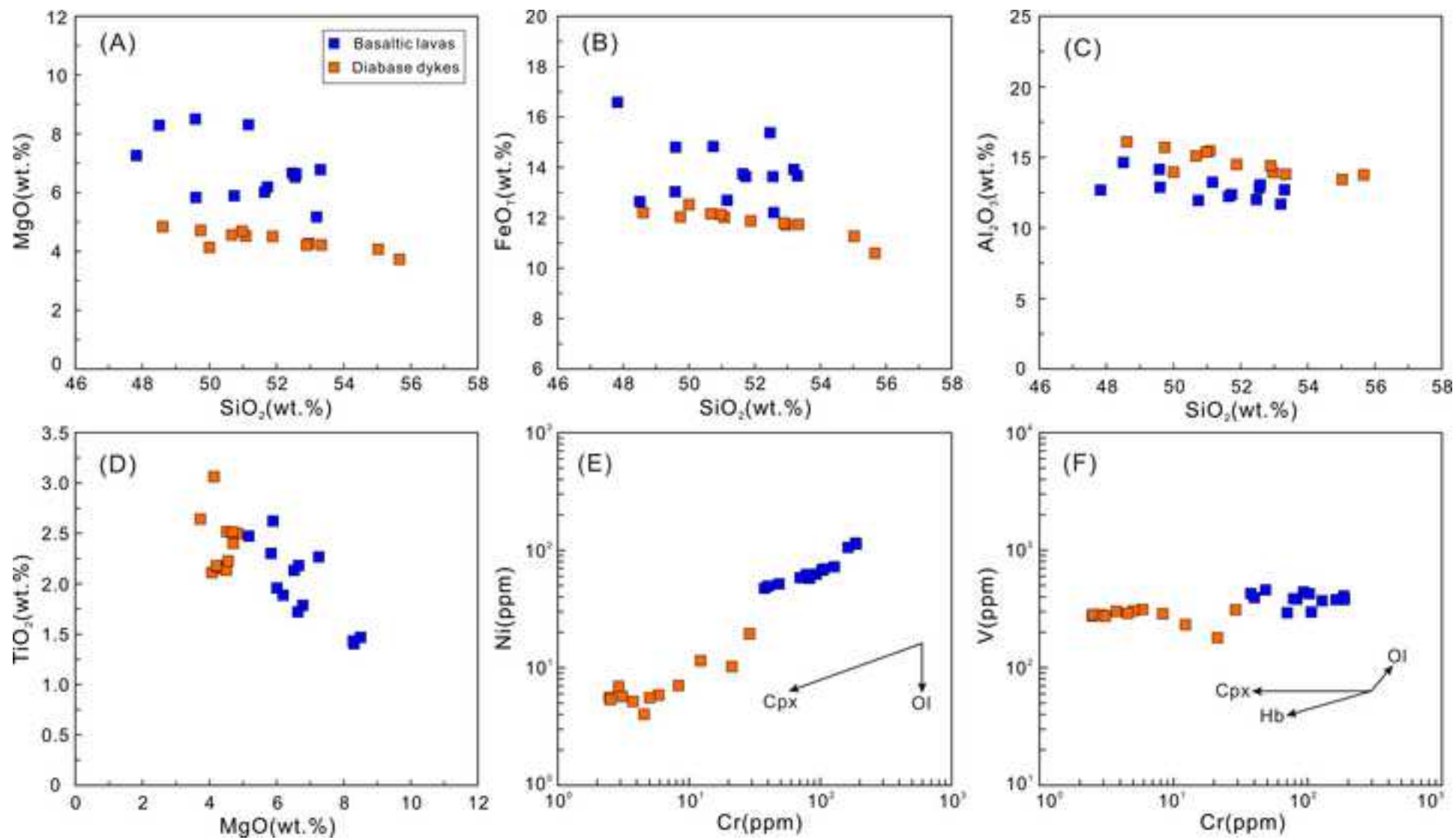


Fig.10-R3

[Click here to download high resolution image](#)

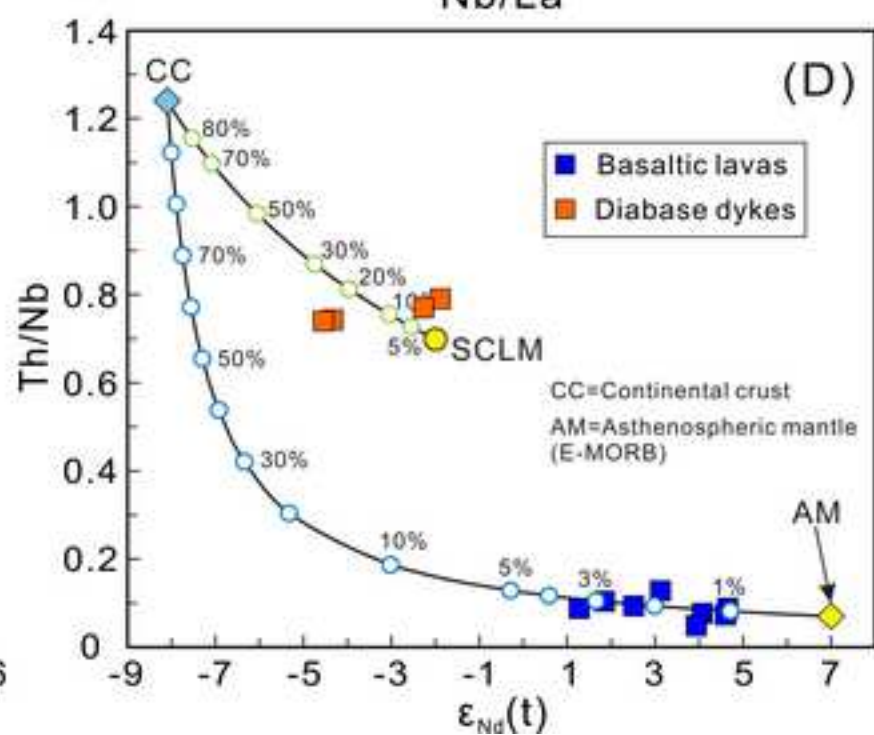
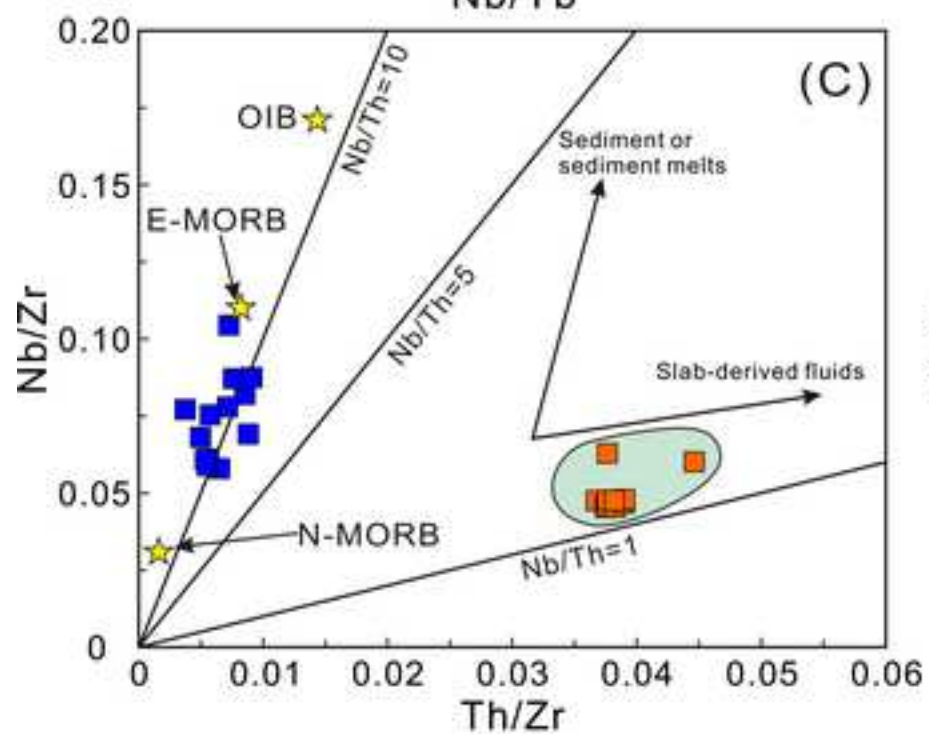
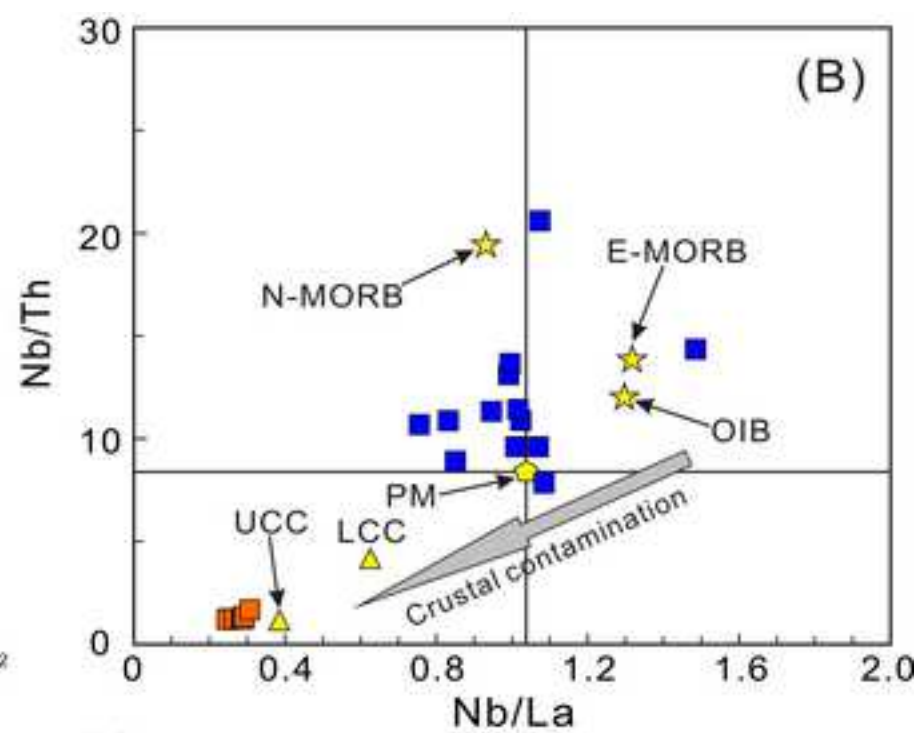
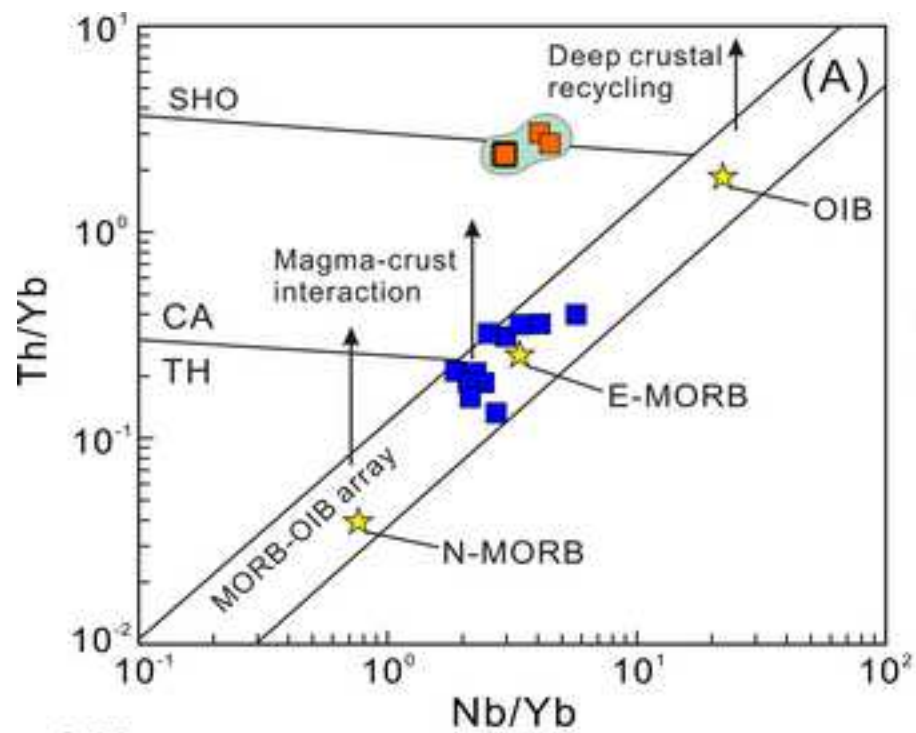
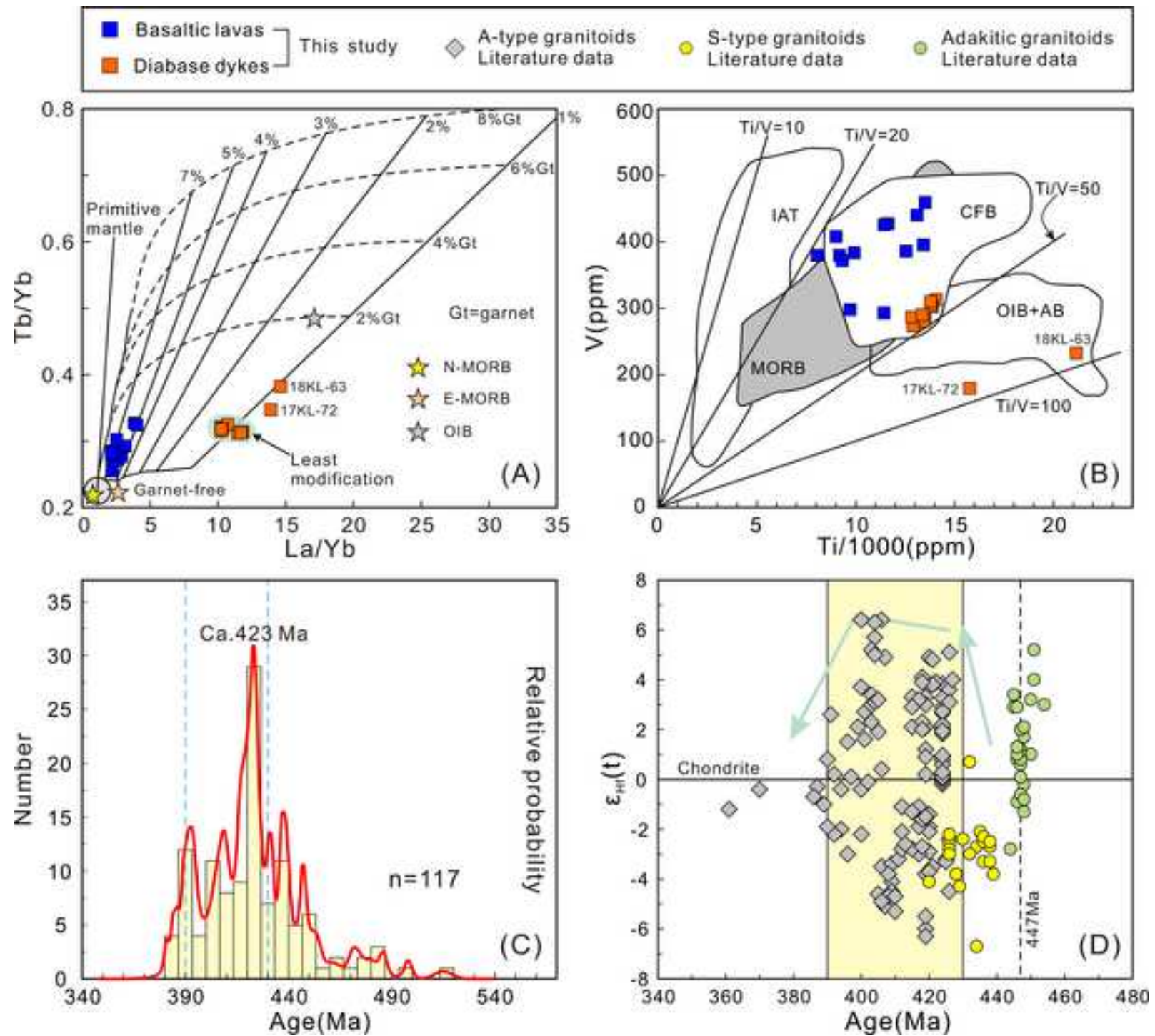
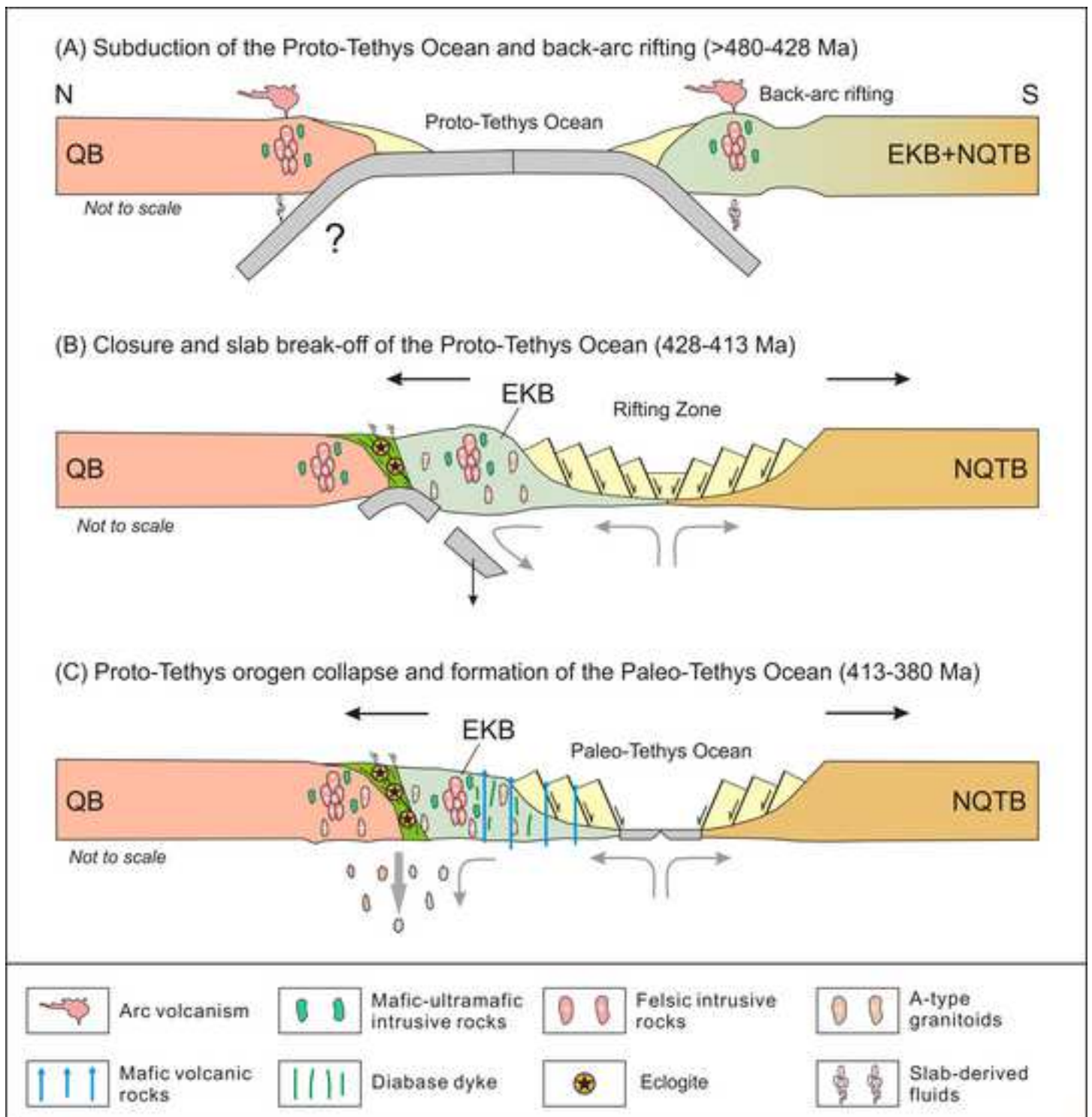


Fig.11-R3

[Click here to download high resolution image](#)





**Table S1-R3**

[Click here to download Supplementary material/Appendix \(Files for online publication only\): Table S1-R3.xlsx](#)

**Table S2-R3**

[Click here to download Supplementary material/Appendix \(Files for online publication only\): Table S2-R3.xlsx](#)

**Table S3-R3**

[Click here to download Supplementary material/Appendix \(Files for online publication only\): Table S3-R3.xlsx](#)



**Table S4-R3**

[Click here to download Supplementary material/Appendix \(Files for online publication only\): Table S4-R3.xlsx](#)

**Table S5-R3**

[Click here to download Supplementary material/Appendix \(Files for online publication only\): Table S5-R3.xlsx](#)

### **Declaration of Competing Interests**

The authors declare that they have no conflicts of personal relationships or financial interests that could have appeared to influence the work reported in this paper.